

## High Density of Strong yet Deformable Intermetallic Nanorods Leads to an Excellent Room Temperature Strength-Ductility Combination in a High Entropy Alloy

Bharat Gwalani<sup>a,b</sup>, Sriswaroop Dasari<sup>a</sup>, Abhishek Sharma<sup>a</sup>, Vishal Soni<sup>a</sup>, Shivakant Shukla<sup>a</sup>, Abhinav Jagetia<sup>a</sup>, Priyanshi Agrawal<sup>a</sup>, Rajiv S. Mishra<sup>a</sup>, Rajarshi Banerjee<sup>a</sup>

<sup>a</sup>Department of Materials Science and Engineering, University of North Texas, Denton, TX 76207

<sup>b</sup>Physical and Computational Directorate, Pacific Northwest National Laboratory, 902, Battelle Blvd, Richland, WA 99354

Corresponding authors: bharatgwalani@pnnl.gov, abhishek.sharma@unt.edu,  
raj.banerjee@unt.edu

### Abstract:

This paper introduces a new microstructural template for high entropy alloys (HEAs), where the face centered cubic (FCC) complex concentrated solid solution is reinforced with a high density of strong, yet deformable, nanorods of an ordered multi-component intermetallic L1<sub>2</sub> compound. Thermodynamic modeling has been employed to design this HEA with a large L1<sub>2</sub> volume fraction. Thermo-mechanical processing by isothermal annealing of the conventionally processed bulk cold-rolled alloy directly at precipitation temperatures, has been applied to produce a high density of uniformly distributed L1<sub>2</sub> nanorods within refined FCC grains, resulting from concomitant recrystallization and discontinuous precipitation processes. The nanorod morphology of the discontinuous L1<sub>2</sub> product has been established from three-dimensional atom probe tomography. The refined grains result in a complete coverage of the microstructure with discontinuously precipitated intermetallic nanorods. This nanorod strengthened HEA exhibits an exceptionally high room temperature yield strength of ~1630 MPa, good tensile ductility of ~15%, and an ultimate tensile strength of ~1720 MPa. Furthermore, a single L1<sub>2</sub> phase alloy, melted based on the precipitate composition in the two-phase FCC + L1<sub>2</sub> HEA, exhibits very high compressive deformability and strain hardenability, unusual for ordered intermetallic

compounds. These results open a new strategy for design of fine-grained microstructures strengthened via ordered intermetallic phases, exploiting the beneficial effects of discontinuous precipitation, for achieving very high room temperature tensile strengths while maintaining good ductility.

**Keywords:** High Entropy alloys, Precipitation Strengthening, Ductility, Twins, High strength

## Introduction

The idea of multiple principle elements resulting in high entropy alloys (HEAs) is now well accepted across the materials research community in developing compositionally-complex alloys for extended tunability of properties [1]. HEAs based on concentrated mixture of various transition elements like Co, Cr, Fe, and Ni have been shown to provide an optimum combination of contrasting properties such as strength and ductility [2,3]. In particular, the heterogeneous microstructures consisting of structural gradation can be an effective method of achieving the strength-ductility synergy as highlighted by Li et al and others [4–6]. Another promising method is precipitation hardening effects in *fcc* based alloys is exhibited by coherent nanostructured L<sub>1</sub><sub>2</sub> precipitates, also referred to as  $\gamma'$  precipitates and are used interchangeably in the current paper. He et al [7] studied the effect of Ti and Al addition on the formation of coherent nanosized L<sub>1</sub><sub>2</sub> and L<sub>2</sub><sub>1</sub> precipitates and their influence on the mechanical properties of FeCoNiCr-based HEA. Liang et al. fabricated FCC-L<sub>1</sub><sub>2</sub> HEA by promoting spinodal decomposition followed by ordering that achieved ultrahigh strength with minimum loss of ductility [8]. *However, it remains very challenging to achieve extremely high yield strength of >1.5 GPa with a reasonable ductility for extreme structural applications.*

The precipitation of ordered intermetallics in an FCC matrix is conventionally achieved by homogenous precipitation of coherent phases like L<sub>1</sub><sub>2</sub>. This results in a uniform distribution of discrete spherical/cubical L<sub>1</sub><sub>2</sub> particles within the FCC matrix. Another pathway to obtain the intermetallic phase is via discontinuous precipitation. However, the discontinuous reaction which nucleates from grain boundaries and grows into the matrix, is typically considered deleterious to mechanical properties [9,10]. For example, in Ni base superalloys, it was reported that the hardness decreases with increasing amount of discontinuous lamellae [9]. Recent studies also report similar effects of discontinuous precipitation where the product is limited to grain

boundary regions [11,12]. The most damaging effects arise from the carbide lamellae resulted from a discontinuous reaction [9]. The interface between carbide lamellae and the FCC matrix act as crack initiation sites affecting the formability and tensile ductility of the alloy [9]. Since the discontinuous reaction occurs by a moving grain boundary, the conventional solution treatment and aging processes restrict the discontinuous product to regions near grain boundaries. Our current work contradicts the established belief of damaging effects of discontinuous precipitation by examining the mechanical properties and deformation behavior of a microstructure entirely comprising of FCC+L<sub>1</sub><sub>2</sub> colonies which exhibits a synergistic improvement of strength and ductility. .

Considering the compositional complexity of these alloys and the number of possible combinations in five or six component space of composition, optimization of alloy composition for achieving a high-volume fraction of strengthening precipitates needs to be guided by computational modeling. Here we report design of an ordered precipitate strengthened alloy based on the FCC-L<sub>1</sub><sub>2</sub> architecture with high strength and ductility. We used an iterative CALPHAD-based solution thermodynamic approach (PANDAT [13] and Thermo-Calc [14]) for alloy optimization, employing the recently developed thermodynamic databases for HEAs. The composition was varied such that the ordered L<sub>1</sub><sub>2</sub> phase is stable up to 1150°C and volume fraction of L<sub>1</sub><sub>2</sub> > 35 % up to 1000°C. The starting point of the alloy optimization was the Al<sub>x</sub>CoCrFeNi HEA system, which has been extensively studied [15]. The FCC based alloys in this system are amenable to strengthening via coherent ordered precipitates (L<sub>1</sub><sub>2</sub>), semi coherent ordered precipitates (B2), and grain boundary strengthening [16–18]. However, the ordered intermetallic L<sub>1</sub><sub>2</sub> phase is only stable at low temperatures, for example, in case of Al<sub>0.3</sub>CoCrFeNi the L<sub>1</sub><sub>2</sub> phase is stable only below 600°C [17]. Therefore, the principal aim of the iterative CALPHAD-based thermodynamic modeling was to use suitable alloy-design approaches to widen the L<sub>1</sub><sub>2</sub> high temperature phase-field while retaining a high-volume fraction, without the addition of high-density refractory elements. Although Co-based superalloys have been developed in the past couple of decades which show high temperature L<sub>1</sub><sub>2</sub> stability [19–21], Co addition increases the raw material cost for commercial applications. Hence, in our current work we employ the high entropy concept to optimize the composition in making it economically more feasible.

After stabilizing a high fraction of strengthening precipitates by compositional optimization, we adopt a unique thermo-mechanical processing route, to design a novel microstructure consisting of intermetallic nanorods uniformly distributed within ultrafine scale (sub-micron) grains of a metallic solid solution. This microstructural template is in contrast with the traditional precipitation strengthened alloys where the strong intermetallic discrete precipitates uniformly distributed within the solid solution matrix are usually either spherical, ellipsoidal or cuboidal. The intermetallic nanorods, in the present case, lead to an exceptionally high yield strength (~1.6 GPa) while retaining substantial tensile ductility (~15%) at room temperature.

## **Experimental and Computational Procedures**

### *Thermodynamic modeling using CALPHAD*

Addition of Al to Co, Cr, Fe, Ni based equiatomic HEA stabilizes L<sub>1</sub><sub>2</sub> phase in the alloy. However, the phase fraction (<20 at. %) and solutionizing temperature (<600°C) for the L<sub>1</sub><sub>2</sub> phase are reported to be low in this alloy system [22]. Ni based superalloys have been developed from past five decades taking advantage of L<sub>1</sub><sub>2</sub> based strengthenabilty, also due to increase in strengthening capability of L<sub>1</sub><sub>2</sub> phase with rise in temperature. Hence, equilibrium stability of L<sub>1</sub><sub>2</sub> at high temperature becomes critical. We used computational thermodynamics (CALPHAD) using TCHEA3 thermodynamic assessment from ThermoCalc [14] to simulate the change in the FCC+L<sub>1</sub><sub>2</sub> phase field by varying the Al, Co, Cr Fe and Ni individually in the alloy. We noticed that minor addition of Ti enhanced the volume fraction and stability of L<sub>1</sub><sub>2</sub> phase and hence, Ti was added to the HEA. The step by step iterative procedure to optimize the composition is provided in supplementary Fig. 1. We see that the optimum composition with respect to the concentration of each of these elements and L<sub>1</sub><sub>2</sub> phase stability and volume fraction is reached at Al<sub>0.2</sub>Ti<sub>0.2</sub>Co<sub>0.7</sub>CrFeNi<sub>1.7</sub>. We then tested the calculated results by casting the alloy and conducting the microstructural characterization.

### *Materials Processing and Characterization*

The alloy was cast in a conventional arc melting furnace by mixing constituent elements, with purity greater than 99.9%, on a water-cooled hearth made of copper in a controlled atmosphere of pure argon. Repeated melting was carried out for five times and the ingot was inverted before every re-melt to ensure chemical homogeneity of the alloy. The cast ingot was ~10 mm in

diameter and ~30 mm in length and was cut into thin slices for characterization. The as-cast samples were solution annealed (SA) at 1200°C for 1 hour for homogenization and solutionization followed by water-quenching to room temperature. These samples were then cold rolled (CR) by 80% reduction in thickness. Cold rolling followed by annealing resulted in recrystallized grain structure and improving compositional homogeneity. A third of the cold rolled alloy was annealed at 1100°C (high temperature annealing, HTA) to recrystallize followed by annealing at 800°C and then water-quenching to room temperature. This condition is called CR-HTA-800. Second part was cold rolled and directly annealed at 800°C and then water-quenched, the CR-800 condition. The remaining third part was directly annealed at 600°C after cold rolling and the water-quenched to room temperature, which is called CR-600 condition in the paper.

Note that the CALPHAD calculations predicts sigma ( $\sigma$  phase) as an equilibrium phase at temperatures below 900°C, in our experimental assessment we did not observe  $\sigma$  phase. Previous studies have reported a prohibitively high barrier for a homogenous nucleation of  $\sigma$  phase in an FCC matrix thus making its precipitation extremely sluggish in FCC HEAs [17,23]. Although a high density of dislocations and defects induced during cold rolling can serve as potent heterogenous nucleation sites for  $\sigma$  phase precipitation [17,23], however, in the current alloy after careful examination at both microscopic and nanoscopic length scales in both CR-800 and CR-600 conditions  $\sigma$  phase was not observed. This may imply a very high barrier to nucleation or this may also indicate a discrepancy in the CALPHAD database associated with this alloy composition.

Macroscopic microstructural characterization and the composition of the arc melted materials was examined by using a FEI Nova-NanoSEM 230<sup>TM</sup> scanning electron microscope (SEM). The SEM was fitted with an energy dispersive X-ray (EDS) detector (EDAX, Model: Apollo X), and a pure Ni standard was used to calibrate it. Alloy samples were scanned several regions in areas of 1\*1 mm<sup>2</sup> to ensure the composition and homogeneity and EDAX's Genesis Spectrum version 6.0 software was used to process the raw data.

Conventional transmission electron microscopy (TEM) studies were carried out with a FEI Tecnai G2 TF20<sup>TM</sup> operating at 200 kV. Precipitate characterization was done using conventional and high angle annular dark field-scanning TEM (HAADF-STEM) modes. To

measure the composition, energy dispersive spectroscopy (Super-X system) equipped on a FEI-TITAN G2 TEM microscope was used in the HAADF STEM mode operating at 300 kV and the results were analyzed with FEI's ES vision software version 6. TEM foils were prepared by a FEI Nova Nano lab 200 dual-beam focused ion beam (FIB) instrument using a Ga ion beam for milling. The ion beam thinning of the samples was done in multiple steps starting from 30 kV ions and finishing with 5 kV ions to reduce the surface damage caused by higher energy ions.

APT required the preparation of needle-shaped samples using the focused ion beam (FIB) method. The FIB-based site-specific specimen preparation was performed with a FEI instrument. The APT experiments were performed in a CAMECA LEAP 5000X XS system using the UV-laser pulse mode to achieve a reasonable yield. The analytical parameters were chosen by performing different test analyses. It was found that 100 pJ for the laser energy and 40 K for the base analysis temperature offered a good compromise; minimizing local magnification effects while retaining a reasonable yield. The data were acquired at an average detection rate of 0.005 ions per pulse. The base pressure was maintained at less than  $10^{-11}$  torr ( $\sim 10^{-9}$  Pa) during the analysis. Reconstruction of the acquired data was performed using the software IVAS 3.6.14 provided by CAMECA. This reconstruction was calibrated based on the initial tip curvature radius measured via SEM.

### *Mechanical Properties*

Dog-bone-shaped tensile specimens with gauge length 5 mm were machined from the rolled and annealed sheets by Electrical Discharge Machining (EDM). Both sides of the specimen were ground using SiC paper to achieve final thickness of  $\sim 0.7\text{--}1$  mm and gauge width of  $\sim 1.0$  mm [24–26]. Tensile tests were performed at an engineering strain rate of  $10^{-3}\text{ s}^{-1}$ . Each test was performed at least three times to ensure consistency; representative results are reported herein. These quasi-static tests used a LVDT (Linear Variable Displacement Transformer) extensometer to perform at least four independent tests to obtain tensile elongation and strength data. The elongation of the gauge length of each sample was measured after testing, and engineering stress–strain curves were calculated from the load-displacement data. Yield strength, ultimate tensile strength, and elongation to failure were determined from the uniaxial tensile stress–strain curves.

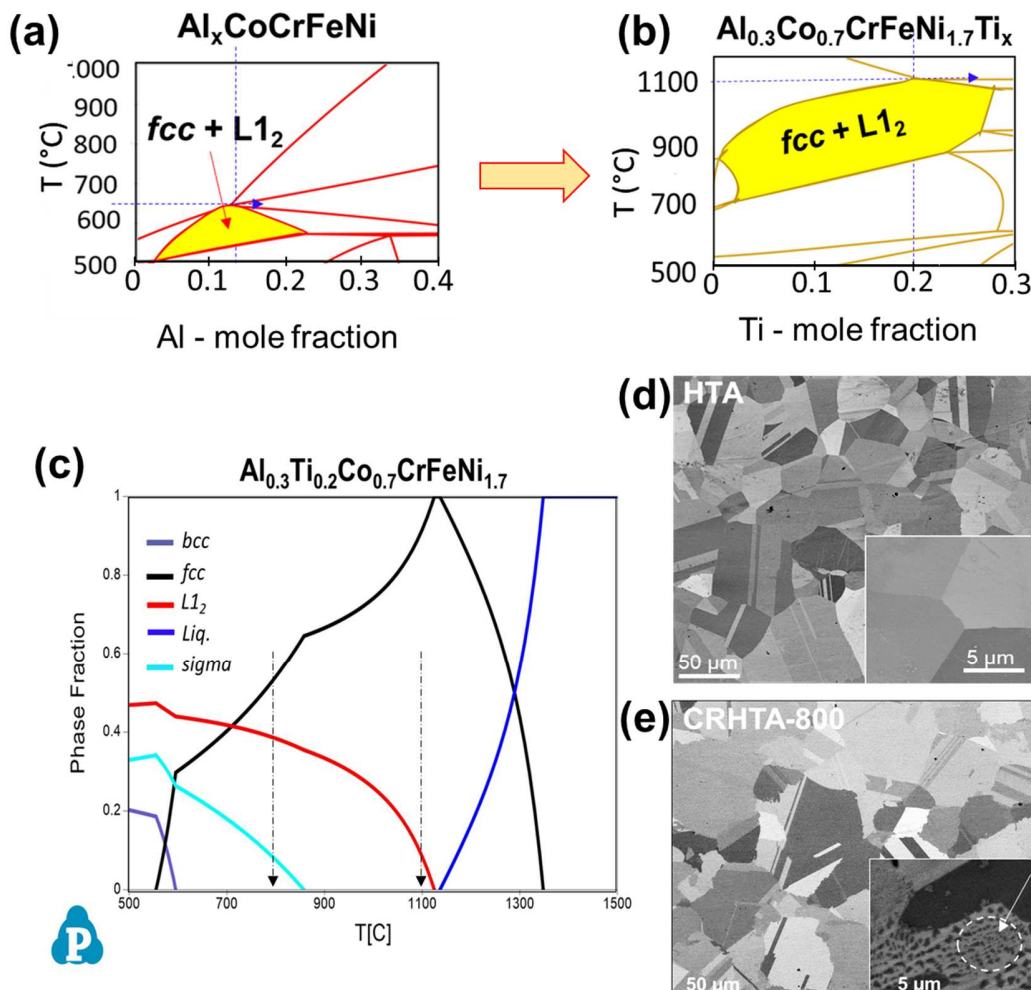
## **Results and Discussion**

### *HEA design guided by solution thermodynamics*

We used an iterative CALPHAD-based solution thermodynamics approach, employing the recently developed thermodynamic databases for compositionally complex alloys like HEAs [13]. The composition was varied such that the L<sub>1</sub><sub>2</sub> phase is stable up to 1100°C with about ~35% volume fraction at 1000°C. Figs. 1(a) and (b) depict the isopleths derived from PANDAT using the PANHEA database [13], showing the first and last steps of the composition optimization process, respectively. Fig. 1(a) shows the isopleth depicting the equilibrium phases as a function of temperature, with varying Al in the CoCrFeNi alloy system. Note that the FCC+ L<sub>1</sub><sub>2</sub> phase field extends up to a temperature of 600°C at the Al concentration of ~2.5 at. %. We use this 2.5 at. % Al to optimize the addition of Fe, Cr, Ni and Ti in maximizing the high temperature stability of L<sub>1</sub><sub>2</sub> phase (Supplementary Fig. S1). Isopleth in Fig. 1(b) shows the equilibrium phases as a function of temperature and Ti content. After several iterations we noted

that the stability of (FCC+L<sub>1</sub><sub>2</sub>), or ( $\gamma$ + $\gamma'$ ) phase field, is extended up to  $\sim$ 1100°C for an alloy with composition Al<sub>0.3</sub>Ti<sub>0.2</sub>Co<sub>0.7</sub>CrFeNi<sub>1.7</sub> with about 35% L<sub>1</sub><sub>2</sub> phase fraction at 1000°C (Fig. 1(c)). After optimization, our alloy composition (Al<sub>0.2</sub>Ti<sub>0.2</sub>Co<sub>0.7</sub>CrFeNi<sub>1.7</sub>) has a theoretical density of  $\sim$ 7.85 gm/cm<sup>3</sup> which is equal to that of mild steel (7.85 gm/cm<sup>3</sup>) and an expected maximum L<sub>1</sub><sub>2</sub> phase fraction of  $\sim$ 50 % (at  $\sim$ 550°C) with temperature stability up to  $\sim$ 1100°C (Fig. 1 (b)).

**Figure 1: CALPHAD based alloy design strategy for the ultra-high strength HEA.** (a) Optimizing Al content based on the isopleth showing phase stability as a function of temperature and Al mole fraction (Al is varied from 0 to 8 at. %) in a CoCrFeNi base alloy. (b) Optimizing Ti content in Al<sub>0.3</sub>Co<sub>0.7</sub>CrFeNi<sub>1.7</sub> base alloy for high temperature phase stability of intermetallic L<sub>1</sub><sub>2</sub> phase (Ti is varied from 0 to 6 at. %). The base alloy was chosen based on the most favorable Co, Cr, Fe and Ni content for a high temperature high strength microstructure (refer to Fig. S1). (c) The phase fraction vs temperature plot for the resultant ultra-high strength HEA. (d) Back



at 1100 °C for 10 mins) condition, the inset shows no visible precipitation). (e) SEM image from the CR-HTA-800 (CR-HTA+ aged at 800 °C for 5 h), the inset has a high magnification view of the fine scale intragranular precipitation.

The alloy with a nominal composition of  $\text{Al}_{0.2}\text{Ti}_{0.2}\text{Co}_{0.7}\text{CrFeNi}_{1.7}$  was cast, cold rolled and homogenized. The SEM micrographs (BSE contrast) from the HTA and CR-HTA-800 condition are shown in Fig. 1 (d) & (e). High magnification SEM imaging (insets of the two figures) shows that the CR-HTA-800 condition consists of a fine scale distribution of spherical/ellipsoidal precipitates uniformly distributed within the *fcc* grains (supplementary Fig. S2). The experimentally observed phase fraction of these precipitates in CR-HTA-800 (~0.35) is close to the predictions from CALPHAD at 800°C (~0.4). An average grain size of  $30 \pm 10 \mu\text{m}$  has been observed in this case, where grain size and texture were estimated by orientation imaging microscopy (OIM). Further details about OIM are provided in the Supplementary Information Fig. S3.

#### Optimization of microstructure by thermomechanical processing

Based on the thermodynamic calculation using CALPHAD, high equilibrium volume-fraction of  $\text{L1}_2$  phase (~50 % phase fraction) can be precipitated at low temperatures (<700 °C), but due to slower diffusion it typically requires a long annealing time to achieve equilibrium. Maintaining a balance between these two factors, we chose to anneal the  $\text{Al}_{0.2}\text{Ti}_{0.2}\text{Co}_{0.7}\text{CrFeNi}_{1.7}$  alloy in the present study at intermediate temperatures of 600°C and 800°C. Annealing the severely cold worked alloy directly at aging temperatures (CR-600 and CR-800) without high temperature recrystallization annealing step results in concurrent recrystallization and precipitation of the strengthening phase ( $\text{L1}_2$  or  $\gamma'$ ), limiting the grain size to sub-micron length scale. The average grain size for both CR-800 and CR-600 conditions was found to be quite similar with an average grain size of  $1.0 \pm 0.20 \mu\text{m}$ , shown in the inverse pole figure (IPF) maps for these two conditions (Figs. 2 (a) and (d)). High magnification SEM images given in Fig. 2(b) from CR-800 and in Figs. 2(e) and (f) from CR-600 show a clear change in precipitate size and morphology between these two conditions. A low magnification SEM-EBSD analysis reveals that after recrystallization, ~31% and ~26.5 % of boundaries are  $\sum 3$  twin boundaries in case of CR-800 and CR-600 conditions, respectively (Fig. S3). In CR-800, the precipitates near the grain boundaries are heterogeneously nucleated and rod-like in morphology, whereas those within the

grains have nucleated homogeneously and are spherical/ellipsoidal (Fig. 2 (b)). Diffraction patterns and dark-field (DF) TEM images confirm that these are L<sub>1</sub><sub>2</sub>-ordered  $\gamma'$  precipitates (Fig. 2 (c) and supplementary Fig. S4).

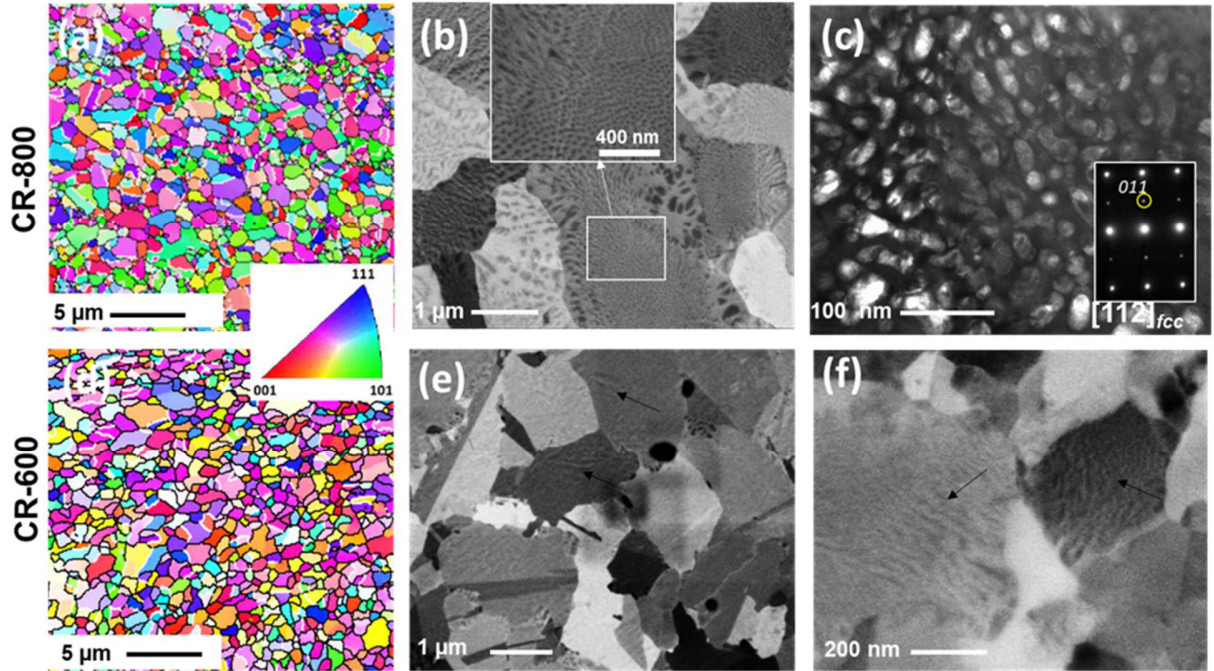


**Figure 2: Fine grained microstructure after thermo-mechanical treatments. (a-c) have the results from the CR-800 while (d-f) have results from the CR-600 conditions** (a) EBSD result with the inverse pole figure map from the (cold rolled for 80% reduction and aged at 800°C for 5 h) CR-800 condition showing the recrystallized grains. (b) A high magnification picture revealing spherical/ellipsoidal precipitation within several grains (inset has intra-grain view for better visualization). (c) Dark Field (DF) image confirming the fine scale precipitates as L<sub>1</sub><sub>2</sub> ( $\gamma'$ ) that are highlighted from the ordered FCC superlattice spot shown in the selected area diffraction pattern (SADP) taken in the [112] zone axis. (d) Ultra-fine grain structure of CR-600 (cold rolled for 80% reduction and aged at 600°C for 50h) condition (d) A high magnification picture of CR-600 condition showing nano-rod precipitation and annealing twins within the ultra-fine grains. (f) Colonies of nano-rod L<sub>1</sub><sub>2</sub> precipitates can be visualized at high magnification SEM as highlighted by the arrows.

In case of the CR-600 condition, the discontinuous microstructure traverses across the entire FCC grains (Fig. 2(f)), unlike in case of the CR-800 condition, wherein the discontinuous colonies are limited to the vicinity of the grain boundaries. Using multimodal characterization tools, we establish in later sections that these elongated precipitates have a rod-like morphology.

Conventional metal processing includes multiple stages of plastic deformation to achieve the final product dimension with a homogenous composition and microstructure. Such severe deformation results in extremely high dislocation densities which necessitates a post-deformation annealing treatment to recover the material's ductility. This post-deformation annealing may also simultaneously help in concurrent precipitation of fine scale semi-coherent or incoherent precipitates [27–30]. Such a dislocation induced heterogenous precipitation provides a handle to tailor the morphology of these coherent precipitates which is traditionally unavailable in the case of homogenous precipitation. Our current work demonstrates that such a morphological modification of the strengthening precipitates from spherical to nano-rod offers substantially higher strength while retaining the inherent ductility.

We conducted a detailed microstructural characterization of the CR-600 condition, to further understand the nano-rod like precipitates. The bright-field (BF) TEM image in Fig. 3 (a) shows a fine-grained microstructure after annealing at 600°C for 50 hours. A significant amount of deformation substructure from the cold rolling step is still retained in the microstructure. This is shown in the dark-field (DF)-TEM image (Fig. 3 (b)), a BF-STEM image (Figs. 3 (c)) and an annular dark-field STEM image (Figs. 3 (d)), all of which reveal the presence of stacking faults along with dislocation segments in these grains. We noted a large number of twin boundaries in the microstructure ( $\Sigma 3$  boundaries), one such boundary is shown in Figs. 3 (e) and (f) which are a pair of dark-field images captured near the [101] zone axis, where a diffraction pattern showing twin-related spots is shown in the inset. We observed a significant fraction of annealing twins during the microstructural evolution of severely deformed cold rolled alloy upon annealing. Annealing twins are often seen in low or medium SFE metals/alloys and can influence the recrystallization process [31]. Field et al. showed that in pure Cu, low temperature recrystallization can enhance the density of annealing twins while restricting the grain growth [31]. Twinning may also influence the phase transformations and mechanical properties in HEAs [30,32]. A self-twinning model has been proposed by Lee et al. in supersaturated FCC materials during the course of precipitation process [33]. This autocatalytic process proceeds with a local stress relaxation concomitant with the precipitation of second phase.

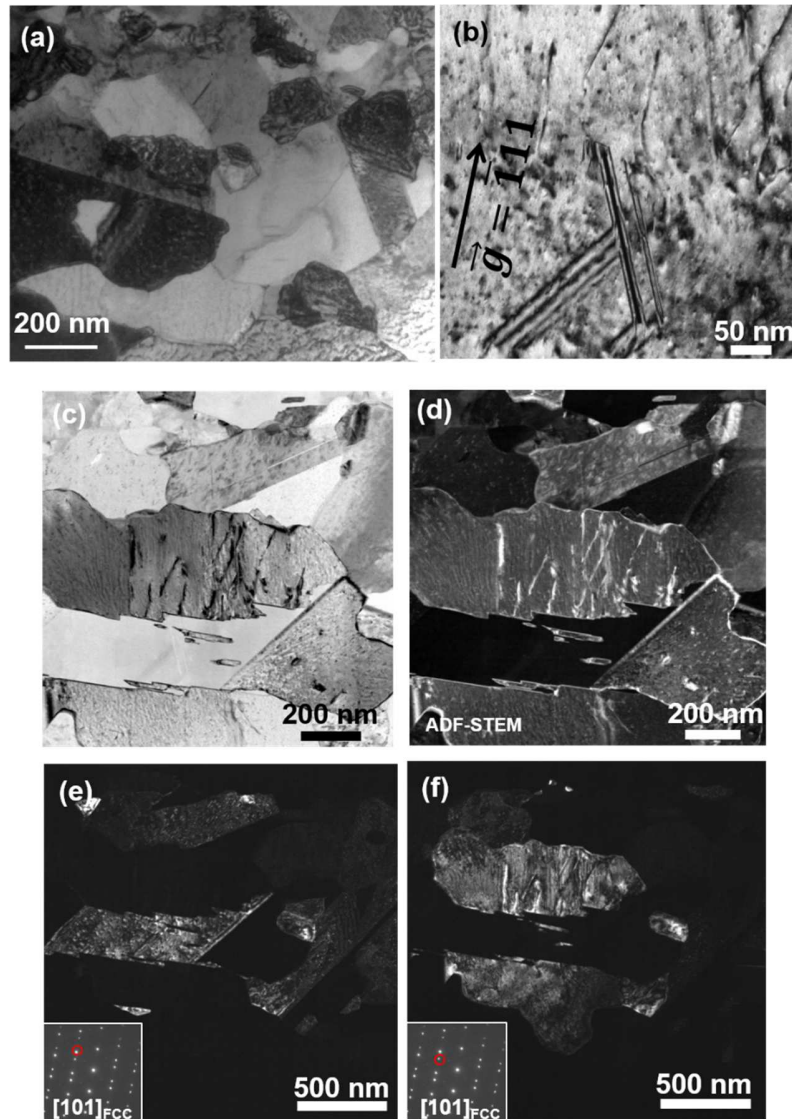


**Figure 3: Detailed TEM results from the CR-600 condition.** (a) Bright Field (BF) TEM image with several recrystallized fine grains. (b) Centered dark field (CDF) TEM image from the same showing presence of stacking faults along with dislocation segments. (c-d) STEM and annular dark-field STEM image showing presence of dislocation substructure retained from the cold rolling step. (e) and (f) are pair of displaced-aperture dark field images captured near [101] zone axis (see insets) showing two neighboring interpenetrating grains in twin orientation with each other.

#### L1<sub>2</sub> ordered $\gamma'$ phase in ultra-fine-grained twinned matrix

Detailed characterization of the L1<sub>2</sub> ordered  $\gamma'$  phase revealed that precipitates appearing lamellar in two dimensional sections (as observed in the SEM and TEM images) are in fact nano-rod shaped. A dark-field (DF) TEM image captured near [001] zone axis in Fig. 4 (a) clearly depicts

the L1<sub>2</sub> ( $\gamma'$ ) nano-rods with an elongated cylindrical shape. Although there exists the classical cube-on-cube orientation relationship between the L1<sub>2</sub> ordered  $\gamma'$  phase and the FCC matrix (see diffraction pattern in the inset of Fig. 4(a)), the serpentine nature of these rods imply that the growth direction of these rods (the long axis of the cylinder) does not lie along any specific crystallographic direction but instead try to be locally normal to the diffusion front sweeping the grain. As the diffusion front associated with the grain boundary changes orientation while moving, so does the nano-rods while maintaining orthogonality with the front resulting in the intertwined serpentine looking nano-rod morphology. Such microstructural features are typically associated with discontinuous precipitation of the reinforcing phase and have been reported in detail previously [9,34]. A high resolution TEM image along the [001] zone axis in Fig. 4 (b) depicts a coherent interface between the matrix and the precipitate (also see supplementary Fig. S5).

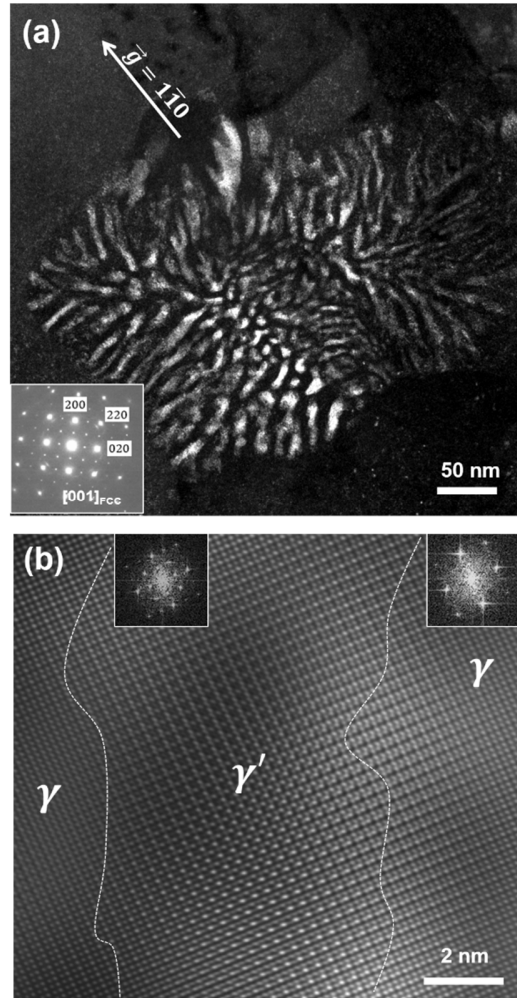


**Figure 4: TEM results from nano-rod precipitates in CR-600:** (a) DFTEM image highlighting the colonies of the nano-rod precipitates in the CR-600 and (b) atomic column high resolution image showing the coherent  $\gamma$ - $\gamma'$  (FCC-L1<sub>2</sub>) phases.

APT investigations further revealed the composition, 3D morphology, and the distribution of these precipitates. The elongated  $\gamma'$  precipitates while being lean in Co, Cr and Fe, are enriched with Al, Ti, and Ni (Fig. 5 (a)). The APT reconstruction of the CR-600 condition illustrates a rod-like morphology of precipitates. These precipitates are oriented orthogonally, where the top region has the rods aligned along the z axis while the bottom region of the needle has the nano-rods aligned along the y axis. An iso-concentration surface with 8 at. % Al was used to demarcate the precipitates from the FCC matrix. In Fig. 5 (b), two different orientations of an APT reconstruction after being rotated by 90° along the z direction, have been shown for a better visualization. The nano-rods have a ~10 nm diameter and an average length of ~100 nm estimated from the APT results. The corresponding composition profiles of all the elements across the FCC/L1<sub>2</sub> or  $\gamma$ / $\gamma'$  interface, are shown as concentration profiles calculated using the proximity histogram method [35] in Figs. 5 (c) with the phase compositions being listed in Table 1. The  $\gamma$  matrix has an average composition of 20.06Ni, 19.89Co, 28.90Fe, 28.08Cr, 2.64Al, and 0.43Ti (at. %) whereas the average composition of  $\gamma'$  is 64.50Ni, 5.70Co, 2.56Fe, 3.45Cr, 12.05Al, and 11.74Ti (at. %). These two compositions estimated from APT analysis show a similar partitioning behavior as predicted by CALPHAD. However, in comparison to the CALPHAD predicted values, the experimentally determined compositions show a supersaturation of matrix with Ni (~7.5 at. %), Al (2.3 at. %), and Ti (0.4 at. %) whereas a supersaturation of  $\gamma'$  precipitates with Co (0.5 at. %), and Cr (2.4 at. %). Also, note the discrepancy in the concentration of Fe is observed to be lower than predicted by 2.4 at. %. The slight disparity between the experimentally determined compositions and the predicted equilibrium compositions can be attributed to three possible reasons. Firstly, annealing at 600°C for 50 h might not achieve thermodynamic equilibrium, and consequently the experimentally measured  $\gamma$  matrix composition may be different than the equilibrium matrix composition predicted by CALPHAD. Secondly, such difference in experimentally observed concentration, and that expected at equilibrium, may also arise from higher supersaturation present in the matrix at 600°C [36]. Lastly, there could be inconsistencies in the CALPHAD databases employed for

making these predictions. The experimental results presented in this study may help in fine tuning these thermodynamic databases. It's worth noting that the matrix as well as the intermetallic  $\gamma'$  both consist of all the five elements. Such a compositional complexity of intermetallic precipitates have been shown to improve their deformability [37].

**Table 1:** Compositions of FCC and L1<sub>2</sub> phases in CR-600 from atom probe tomography.

| Phase                        |         | Ni    | Co    | Fe    | Al    | Ti    | Cr    |
|------------------------------|---------|-------|-------|-------|-------|-------|-------|
| Matrix<br>(APT)              | At.%    | 20.06 | 19.89 | 28.90 | 2.64  | 0.43  | 28.08 |
|                              | Sigma % | 0.06  | 0.02  | 0.03  | 0.02  | 0.08  | 0.03  |
| L1 <sub>2</sub><br>(APT)     | At.%    | 64.5  | 5.70  | 2.56  | 12.05 | 11.74 | 3.45  |
|                              | Sigma % | 0.4   | 0.03  | 0.02  | 0.04  | 0.04  | 0.02  |
| Matrix<br>(CALPHAD)          | At.%    | 12.4  | 21.10 | 31.30 | 0.33  | 0.01  | 34.80 |
| L1 <sub>2</sub><br>(CALPHAD) | At.%    | 64.4  | 5.20  | 3.20  | 13.90 | 12.30 | 1.00  |

Summarizing the microstructure of CR-600 alloy, the low temperature recrystallization limited *fcc* grain growth, along with high density of annealing-twins, and a discontinuous precipitation of nano-rod like  $\gamma'$  dominates over the more commonly observed homogeneous  $\gamma'$  precipitation within *fcc* matrix grains [9]. This discontinuous precipitation of  $\gamma'$  throughout the grain is a novel microstructural template which is introduced in the current work and will be discussed in the following section.

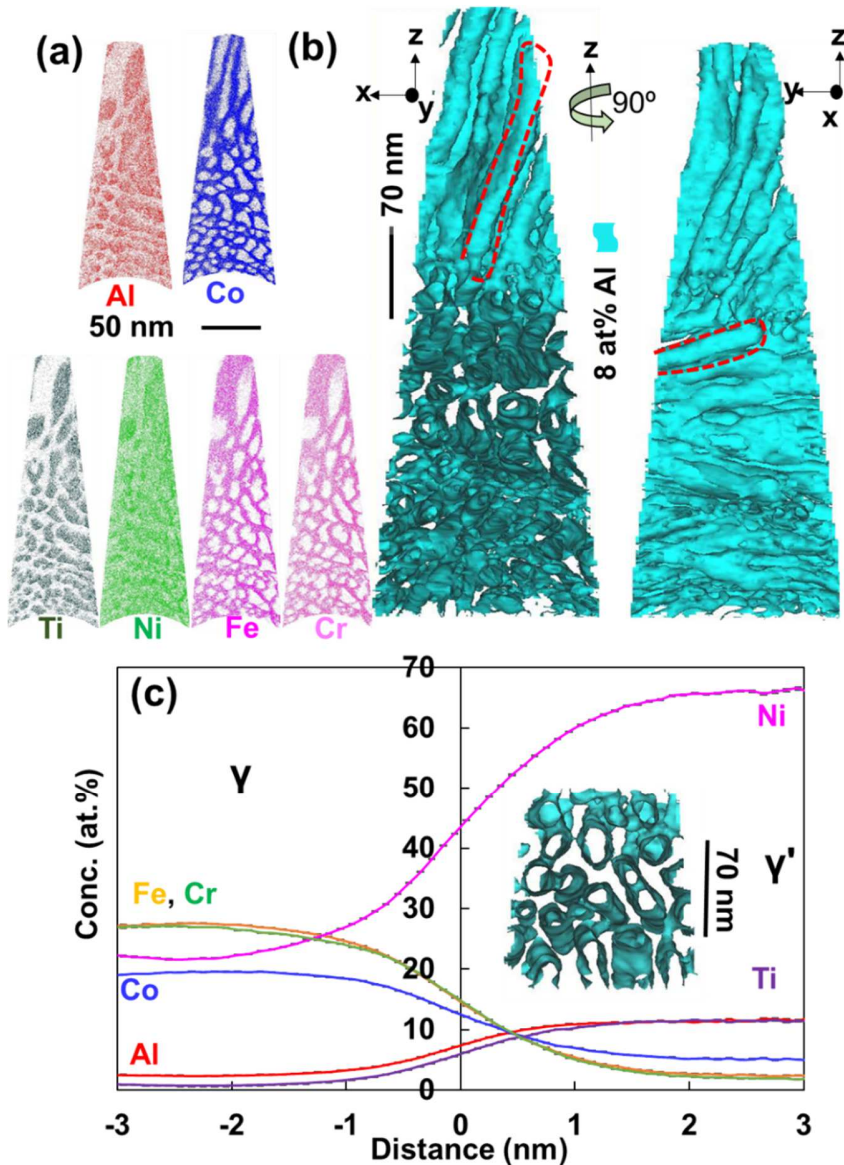


**Figure 5: APT results from nano-rod precipitates in CR-600:** (a) 10 nm thin slices from the APT reconstruction showing the distribution of elements - Al, Co, Fe, Cr and Ni (b) An iso-concentration surface is used to delineate the Al rich (>8 at. % Al) from Al lean regions. The Al rich regions highlight the nano-rod precipitates. (c) Compositional profiles (proximity histograms) of each element across the FCC- L12 ( $\gamma$ - $\gamma'$ ) interface.

Discontinuous precipitation of coherent  $\gamma'$  nano rods

When a supersaturated single-phase solid solution is annealed within a two-phase phase-field, the supersaturation of this solid solution is rejected by a solid-state reaction either involving homogenous precipitation or heterogenous precipitation [38]. The homogeneous nucleation of precipitates occurring throughout the matrix is termed as continuous precipitation (CP). The heterogenous nucleation aided by a migrating grain boundary/reaction front results in a phenomenon called discontinuous precipitation (DP) [9]. There are broadly two types of discontinuous reaction mechanisms proposed in the literature. The first mechanism involves precipitation induced boundary migration and the second mechanism is based on precipitation on moving grain boundaries. In the latter, the driving force for grain boundary migration can arise from stored energy (recrystallization) or reduction in interfacial energy (grain growth). In the current alloy, the discontinuous reaction is expected to have followed the second mechanism (Fig. 6). In this mechanism, the thermally activated motion of a grain boundary sweeps the solute in its path resulting in accumulation of solute at the grain boundary leading to the formation of  $\gamma'$  nuclei along the *fcc* grain boundary. The concentration gradient across the boundary drives further movement resulting in bowing of the grain boundary due to pinning by precipitate nuclei. Simultaneously, the nuclei of the precipitates grow because of the accumulation of fresh solute from the migrating reaction front. This process repeats itself, ultimately leading to a microstructure consisting of nano-rod shaped  $\gamma'$  colonies within the FCC matrix seen in CR-600 condition of our alloy (Fig. 6(e)).

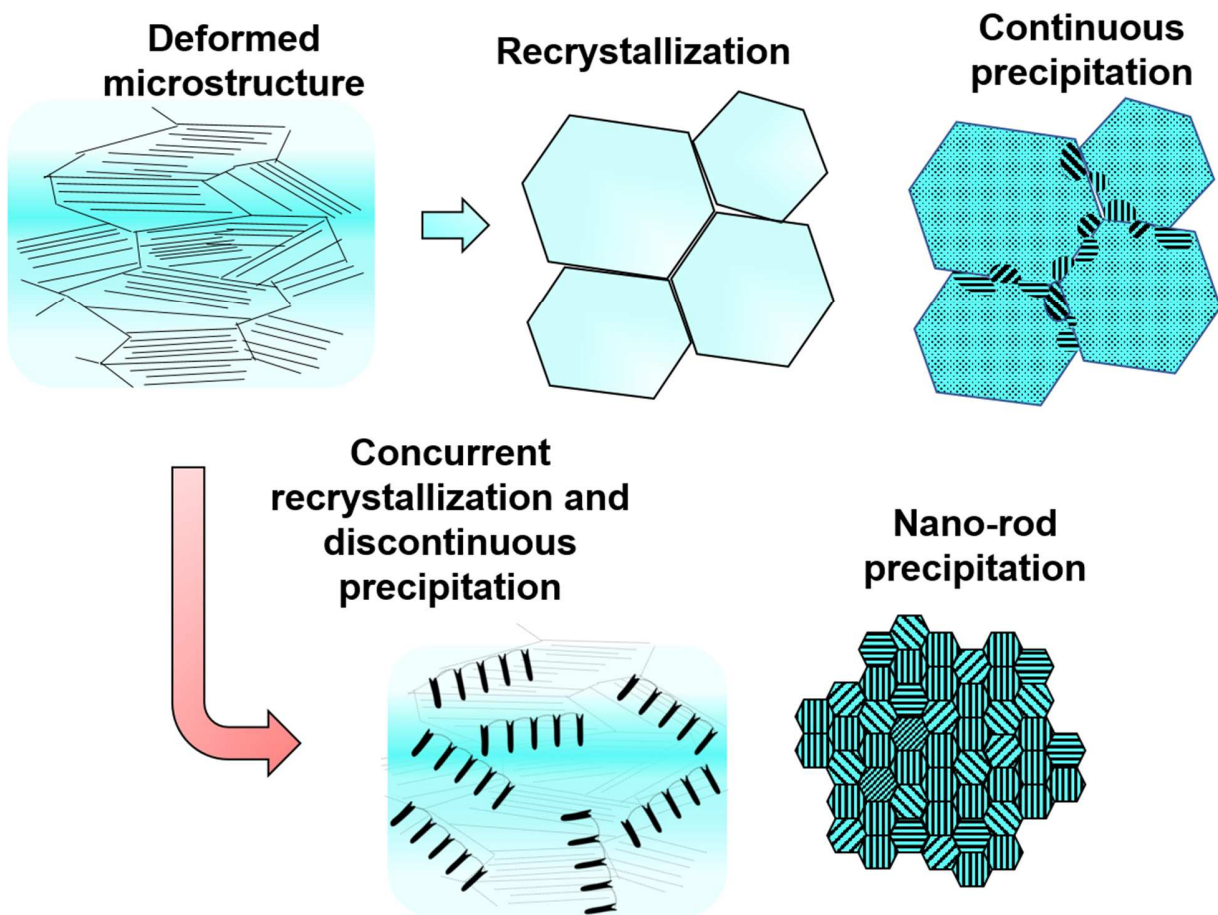


**Figure 6.** Schematic showing the precipitation sequence for nano-rod shaped precipitates.

(a) represents a highly deformed condition of a super saturated solid solution, (b) after annealing at temperature above homogenization temperature resulting in homogeneous recrystallization (c) precipitation annealing and formation of homogeneous precipitates, with minor discontinuous precipitation limited to regions near grain boundaries (seen in CR-800) (d) When severely deformed alloy condition is annealed at lower temperature where nano-rod precipitation occurs on the migrating boundaries (e) a later stage where recrystallization coupled with nano-rod precipitation takes over the whole microstructure.

In the CR-HTA-800 condition (Fig. 1 (e)) which has undergone cold rolling (Fig. 6 (a)) followed by recrystallization at high temperature ( $1150^{\circ}\text{C}$ , Fig. 6 (b)) prior to annealing at  $800^{\circ}\text{C}$ , the starting condition consists of coarse *fcc* grains in which the grain boundary movement is limited. This results in a microstructure with mostly continuous precipitation, leading to a homogeneous distribution of precipitates within the FCC matrix (Fig. 6 (c)). In contrast, for the CR-600

condition, the 80% cold-rolled condition is directly annealed at a lower temperature of 600°C, resulting in concurrent recrystallization of the FCC grains and  $\gamma'$  nano-rod precipitation within these grains (Fig. 6 (d)). Therefore, as the FCC grains recrystallize, the resulting rapid motion of the grain boundaries sweeping the solute elements, is coupled with concurrent  $\gamma'$  precipitation at these boundaries. These precipitates grow themselves as well pin the boundaries, leading to discontinuous  $\gamma'$  precipitation, resulting in rod-like colonies of FCC +L1<sub>2</sub> or  $\gamma/\gamma'$  permeating the entire microstructure (Fig. 6 (e)).

However, it must be noted that the nano-rod morphology of L1<sub>2</sub> could also be a result of growth along dislocations. Many solid-state phase transformations are assisted by heterogenous nucleation sites such as dislocations. The size scale and morphology of the FCC+L1<sub>2</sub> colonies in the current alloy, however, suggests a discontinuous precipitation reaction. This speculation is further supported by the presence of large driving force for recrystallization (from cold work) and precipitation of L1<sub>2</sub> phase (refer to Fig. 1(c)). Additionally, to confirm the possible role of dislocations in nucleating rod-like precipitates, we have characterized the microstructure of the alloy in partially recrystallized condition after cold rolling to ~60% reduction in thickness, followed by annealing at 600°C for 50hrs. The results from this study are shown in Fig. 7 below. The low magnification backscattered SEM micrograph in Fig. 7(a) shows recrystallized and non-recrystallized regions (separated by a red line on the figure). The high magnification picture in 7(b) shows the discontinuous reaction front formed by coupled recrystallization of FCC grains, and L1<sub>2</sub> precipitation, in the wake of the moving grain boundary resulting from the recrystallization. The rod-like L1<sub>2</sub> precipitates are visible in the recrystallized regions whereas homogeneously distributed spherical L1<sub>2</sub> precipitates are visible in the non-recrystallized region, with the retained cold work. Another example of the change in precipitate morphology between recrystallized and non-recrystallized regions is shown in Fig. 7(c). The spherical precipitates in the non-recrystallized region are clearly revealed from the micrograph recorded from this region (Fig. 7(d)). Further, TEM analysis of this condition is shown in Figs. 7(e-f). Fig. 7(e) shows the spherical precipitates revealed by a dark field image recorded from the non-recrystallized region. Similarly, a dark field image recorded from the recrystallized region, shown in Fig. 7(f), clearly reveals rod-like precipitates.

The non-recrystallized regions in the SEM images (Figs. 7(a-c)) show some strain contrast due to remnant dislocation density from cold work. Despite the high dislocation density, the L<sub>1</sub><sub>2</sub> precipitates were not found to have a rod-like morphology within these regions. These results establish that the pre-existing dislocations are not likely to be responsible for the rod-like morphology of the L<sub>1</sub><sub>2</sub> precipitates. Instead, discontinuous precipitation appears to be the mechanism behind nano-rod morphology.

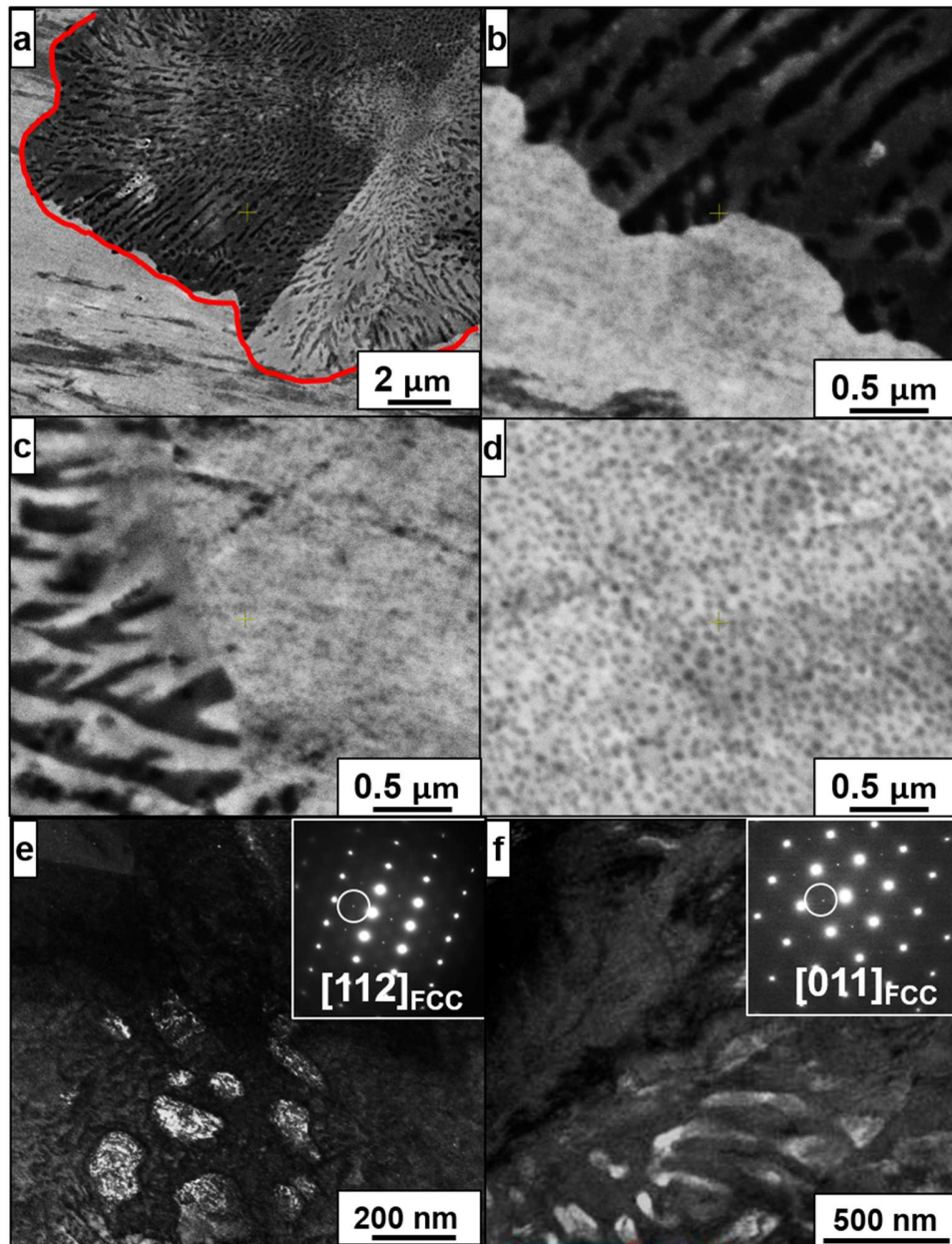


**Figure 7:** (a-d) Backscattered SEM micrographs from the alloy rolled to 60% and annealed at 600°C for 50 hrs; (a) The partially recrystallized microstructure in this condition. The interface between recrystallized and non-recrystallized regions is marked by a red line on the figure. (b) Discontinuous reaction front formed by concurrent recrystallization and precipitation. The rod-like L<sub>1</sub><sub>2</sub> precipitates are visible in the recrystallized regions whereas the spherical L<sub>1</sub><sub>2</sub> precipitates are visible in non-recrystallized region. (c) Change in precipitate morphology from recrystallized to non-recrystallized regions recorded from another region. (d) The non-recrystallized region containing spherical precipitates. (e-f) TEM analysis of the same condition; (e) Spherical precipitates revealed through dark field image recorded from non-recrystallized region. Corresponding diffraction pattern is shown as an inset. (f) Dark field image recorded from recrystallized regions shows the rod-like precipitates. Corresponding diffraction pattern is shown as an inset.

#### Mechanical Properties

The mechanical behavior under quasi-static tensile loading (strain rate  $\sim 10^{-3}$  sec<sup>-1</sup>), for the different thermo-mechanically processed conditions of our HEA, have been summarized in Figs. 8(a-c)). The engineering and true stress-strain plots of the conditions (Figs. 8(a-b)) show that the CR-HTA-800 condition (with continuous precipitation of spherical  $\gamma'$ ) has a yield strength of ~980 MPa with UTS ~1420 MPa and 22% plastic strain to failure. The CR-800 condition exhibits a yield strength ~1370 MPa, UTS ~1540 MPa and 12% ductility. The CR-600 condition exhibits a rather remarkable combination of strength and ductility with a yield strength ~1630 MPa, UTS ~1720 MPa and 15% tensile ductility. Note that the strength and ductility both are higher for the CR-600 condition as compared to the CR-800 condition (Fig. 8 (a)). All conditions exhibit a distinct four-stage work-hardening response, which is very characteristic of a low SFE material (Fig. 8 (c)) [39–41].

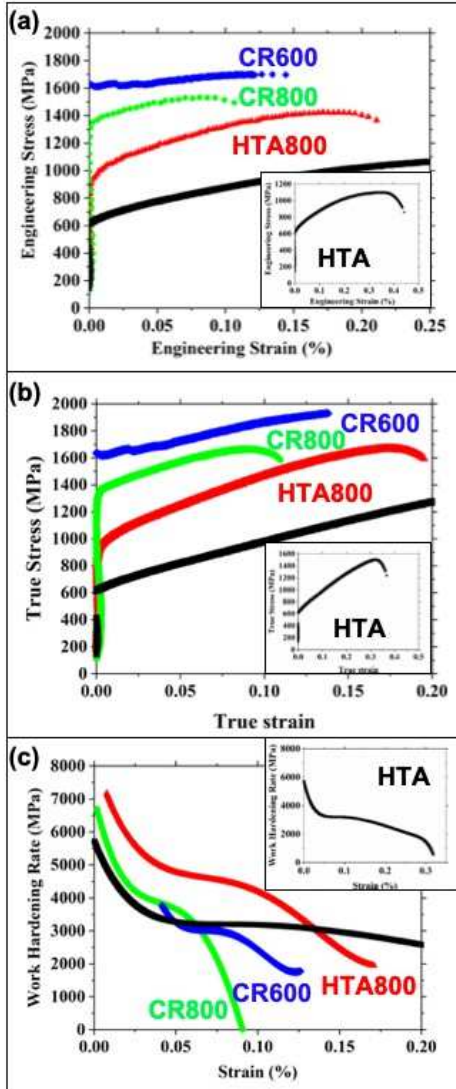


**Figure 8. Mechanical performance of the alloy under different conditions:** (a) The tensile engineering stress vs strain curves, (b) true stress vs strain curves (c) and work-hardening plots for the CR-HTA, CR-HTA-800, CR-800 and CR-600 conditions. The work hardening plot shows a multi-stage hardening mechanism activated as a function of plastic strain.

#### Estimation of the tensile yield strength

A simple strengthening model has been employed to estimate the various contributions to the yield stress of this nanorod strengthened HEA in the CR-600 condition. The typical strengthening mechanisms contributing to the tensile yield stress ( $\sigma_y$ ) of a precipitation strengthened alloy are lattice-friction stress ( $\sigma_o$ ), grain boundary or Hall-Petch strengthening

( $\sigma_{HP}$ ), solid-solution strengthening ( $\sigma_S$ ), dislocation strengthening ( $\sigma_D$ ), and precipitation strengthening ( $\sigma_P$ ), as given in equation (1).

$$\sigma_y = \sigma_o + \sigma_{HP} + \sigma_S + \sigma_P \quad (1)$$

We have developed a Hall-Petch relationship for the CoCrFeNi HEA in a separate study [42], resulting in a friction stress ( $\sigma_o$ ) value of ~156 MPa and Hall-Petch strengthening co-efficient, k ~684 MPa $\sqrt{\mu\text{m}}$ . The grain boundary or Hall-Petch strengthening is given by  $k/\sqrt{D}$ , where D is grain diameter. This contribution was calculated to be ~684 MPa for the CR-600 condition (~1  $\mu\text{m}$  average grain size). Assuming that Al and Ti are solute elements added to the CoCrFeNi base matrix, the solid solution strengthening contribution can be calculated according to the Fleischer model [43] given below:

$$\sigma_{SS} = M \cdot \frac{G \cdot \varepsilon_s^{3/2} c^{1/2}}{700} \quad (2)$$

where M = 3.06 is Taylor factor, to convert shear stress to flow stress for a polycrystalline *fcc* microstructure, G is the shear modulus ~84 GPa, assumed to be similar to CoCrFeNi [44], c is concentration of solute and  $\varepsilon_s$  is defined as:

$$\varepsilon_s = \left| \frac{\varepsilon_G}{1+0.5\varepsilon_G} - 3 \cdot \varepsilon_a \right| \quad (3)$$

where size misfit parameter,  $\varepsilon_a = \frac{1}{a} \frac{\partial a}{\partial c}$  and modulus misfit parameter,  $\varepsilon_G = \frac{1}{G} \frac{\partial G}{\partial c}$ . Here, a is lattice parameter of the base alloy, CoCrFeNi. Since the modulus misfit contribution is usually negligible compared to size misfit contribution,  $\varepsilon_s$  can be written as  $|3 \cdot \varepsilon_a|$  [45]. Since second phase precipitation is involved in all conditions, the *fcc* matrix composition determined from APT (refer to Table 1) has been used for calculating the solid solution strengthening. The lattice parameters for CoCrFeNi and the *fcc* matrix composition have been derived from *fcc* lattice parameters of individual elements, based on a simple rule of mixtures. Thus, the solid solution strengthening contribution arising from the addition to Al and Ti to CoCrFeNi was calculated to be ~37 MPa. This is consistent with multiple reports in the literature indicating that the tensile yield strength of Al and Ti containing alloys is not substantially different from the base alloys [46,47].

Precipitation strengthening contribution can be estimated based on the L1<sub>2</sub> phase fraction determined to be ~45% from APT. Assuming that precipitation strengthening is a result of dislocations shearing spherical L1<sub>2</sub> particles, this contribution has been estimated using equation (4) [48].

$$\sigma_P = M \cdot 0.81 \frac{\gamma_{APB}}{2b} \left( \frac{3\pi f}{8} \right)^{\frac{1}{2}} \quad (4)$$

where  $\gamma_{APB}$  is the anti-phase boundary (APB) energy of L1<sub>2</sub> precipitate, b is burger's vector, f is the volume fraction of L1<sub>2</sub> precipitates in the *fcc* matrix. Vittori and Mignone [49] established a relationship between APB energy and Ti/(Ti+Al) ratio for L1<sub>2</sub> precipitates, from a combination of first principles calculations and experimental observations. Based on the composition of L1<sub>2</sub> shown in Table 1, the Ti/(Ti+Al) ratio in these precipitates was found to be ~0.49. Accordingly, the APB energy ( $\gamma_{APB}$ ) of 0.13 J/m<sup>2</sup> (refer to Fig. S3) was adopted for this alloy. The Burger's vector was calculated to be 0.253 nm based on the *fcc* lattice parameter of 3.5801 Å obtained from XRD. Based on these parameters, the precipitation strengthening in CR-600 condition was calculated to be  $\sigma_P = 463$  MPa. Based on the change in area on slip plane intersected by rod-like precipitates, Kelly [50] calculated that the strengthening from rod-like particles can be 1.75 times more effective than the spherical particles of the same volume fraction. Based on the Kelly model, the expected precipitation strengthening calculated for the nanorod-like precipitates in the current study is ~810 MPa (463 MPa x 1.75). Therefore, the combined contribution from  $\sigma_o$  (156 MPa),  $\sigma_{HP}$  (684 MPa),  $\sigma_S$  (37 MPa),  $\sigma_P$  (810 MPa) in CR-600 can be estimated to be ~1687 MPa. This value is in good agreement with the experimentally observed yield strength of 1630 MPa.

#### Deformation mechanisms in CR-600 condition

A more detailed investigation of the plastically strained microstructures has been carried out to decipher the deformation mechanisms operative in the CR-600 condition that demonstrated the best strength-ductility combination in the present study. Low magnification and high magnification DF-TEM images (Fig. 9 (a-b) respectively) from a sample deformed to fracture ( $\epsilon_p \approx 15\%$ ) show a very homogenous distribution of dense dislocation tangles through-out the grain. The DF-TEM image (Fig. 9 (c)) acquired from the superlattice spot corresponding to the same region shows poor contrast from the  $\gamma'$  indicating significant scattering of electrons due to

dense dislocation network completely surrounding as well as shearing the  $\gamma'$  nanorods extensively. This further establishes the homogeneity of the dislocation substructure developed during plastic deformation, which is critical for ensuring uniform strain hardening and eventually ductility in the material [39]. Some grains also show presence of extremely fine deformation twins as seen in Fig. 9 (d-e), which is a BF-TEM image and Fig. 9 (f) which is an HR-TEM image of this twin.

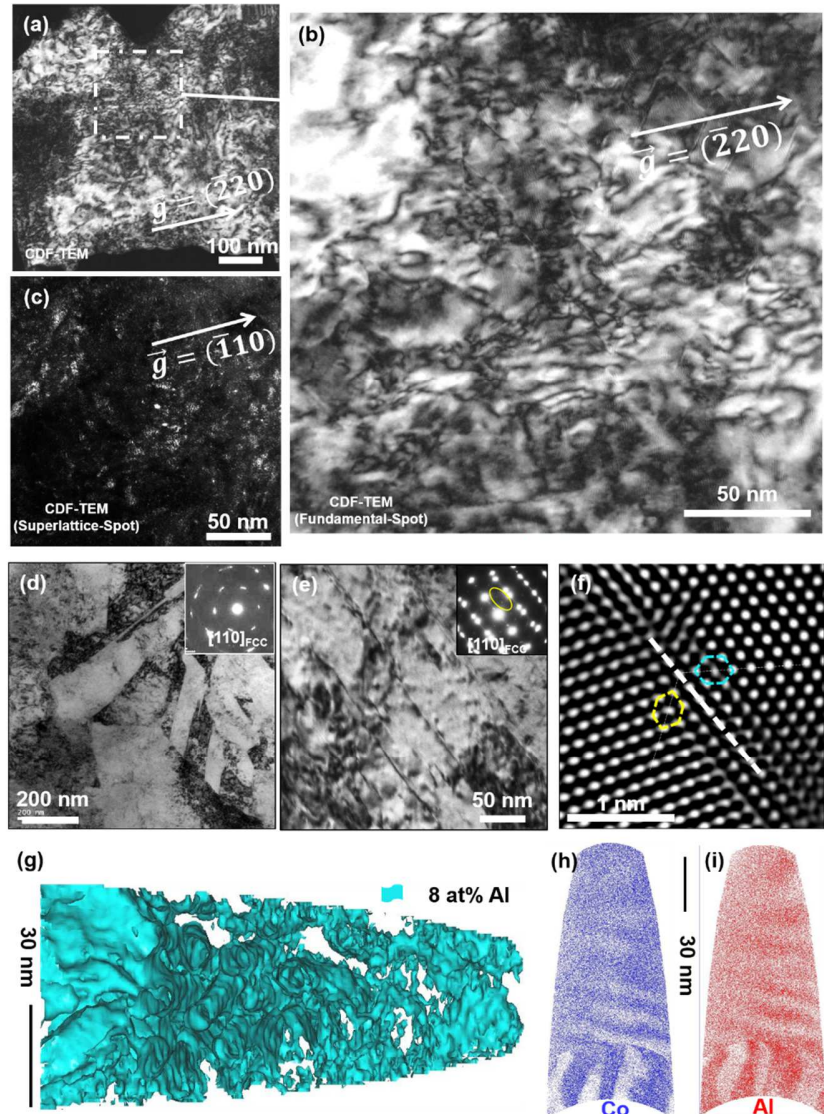


**Figure 9. Deformed microstructure of CR-600.** (a) Low magnification and (b) High magnification CDF-TEM image from a sample deformed to fracture ( $\epsilon_{pl} \approx 22\%$ ) showing a very homogenous distribution of dense dislocation tangles through-out the grain. (c) CDF-TEM image acquired from the superlattice spot corresponding to (b). Poor contrast from  $\gamma'$  indicates

significant  $\gamma'$ -dislocation interaction during deformation. (d) Low mag BF-TEM image along with the corresponding DP (see inset) indicates significant grain rotation in the deformed microstructure. (e) BF-TEM image shows presence of extremely fine deformation twins in some grains. (f) HRTEM image showing one such twin-interface. (g-i) APT results from the deformed microstructure in the CR-600 highlighting the shearing of the precipitates and smudging of the phase boundaries.

As indicated, the principal deformation mechanism is homogenous dislocation-mediated plasticity eventually leading to dislocation-dislocation interactions along with extensive shearing of precipitates. The homogeneity of the dislocation slip ensures uniform strain hardening over the course of tensile deformation which ultimately translates into good ductility. In addition to dislocation-mediated plasticity, some amount of strain is also being accommodated by deformation twinning. Nano-twinning and dislocation slip have been seldom reported in single phase medium SFE HEAs resulting in enhanced plasticity and strain hardenability of the alloys [51,52]. It should be noted that the diffraction pattern in Fig. 9 (e, inset) shows twin reflections from both the FCC matrix as well as the  $\gamma'$  precipitates, indicating that these deformation twins pass through both the disordered FCC matrix as well as the ordered  $\gamma'$  precipitates. The mechanism of deformation twinning in nickel-base superalloys is closely associated with that of super extrinsic stacking faults (SESF) formation [53]. Whereas passage of a single Shockley partial along a {111} type plane results in creation of a SESF within the L<sub>1</sub><sub>2</sub> ordered precipitate, passage of multiple Shockley partials on adjacent {111} type planes result in formation of a deformation twin [54–57]. Interestingly, in case of nickel-base superalloys, such mechanisms are observed during creep deformation at high stresses and intermediate temperature. Activation of such mechanisms at room temperatures and easy transmission of twins across a  $\gamma$ - $\gamma'$  interface indicates low SESF energy associated with the L<sub>1</sub><sub>2</sub> composition in our case. These results also point towards good strain-hardenability of the L<sub>1</sub><sub>2</sub> phase which is presented in the next section.

APT analysis was also carried out from this deformed sample (Fig. 9 (g-i)). An 8 at. % iso-concentration surface, shown in Fig. 9 (g), shows a highly “crinkled”  $\gamma$ - $\gamma'$  interface between the FCC matrix and the L<sub>1</sub><sub>2</sub> ordered nano-rod colony after plastic deformation, as compared to a very well-defined and sharp  $\gamma$ - $\gamma'$  interface in the undeformed condition (Fig. 5(b)). This indicates extensive shearing of the  $\gamma'$  nano rods during the homogenous dislocation slip. The Co and Al ion map reconstruction (Fig 9(h) and (i), respectively) show clear loss of compositional partitioning along the top part of the nano-rod colony, amongst the precipitate and matrix following plastic

deformation. We consistently observed such compositional intermixing in multiple APT reconstructions of tips extracted from the deformed sample. The diffuse compositional partitioning promotes uniform strain transfer across the coherent interfaces during deformation and thus ensuring good ductility. Figs 10 (a-b) show two-dimensional thermal maps of Al (0 to 13 at. %) and Co (0 to 20 at. %) from an undeformed CR-600 condition. A very clear and sharp partitioning of these elements across the  $\gamma$ - $\gamma'$  interface is evident. A one-dimensional compositional profile along a cylindrical geometry across a precipitate-matrix-precipitate region depicts the same (Fig 10 (c)). For comparison, a similar analysis on the deformed specimen from the CR-600 condition is shown in Fig. 10(d-e), which are the two-dimensional thermal maps of Al (0 to 7 at. %) and Co (0 to 18 at. %). We clearly see a lack of clear demarcation between precipitate and matrix in the deformed alloy manifesting as compositional mixing of the matrix and the precipitate. A one-dimensional cylindrical profile across precipitate-matrix-precipitate from the deformed condition provides a direct comparison with a similar profile from the undeformed condition, shown in Fig. 10 (c). Although such compositional mixing during plastic deformation has been observed previously in multiple systems [58–62], it has been primarily associated with high strain-rate deformation. Localized adiabatic shearing during such high strain rate deformation may lead to temperatures beyond solvus, leading to precipitate dissolution along these adiabatic shear-bands (ASB's), resulting in compositional mixing. While the present experimental observations clearly indicate strain-induced intermixing between the intermetallic precipitates and the matrix at much lower strain rates ( $\sim 10^{-3}$  sec $^{-1}$ ), further detailed investigation and analysis are required for rationalizing these unusual observations. However, it should be noted that such an intermixing presumably promotes slip homogeneity which in turn leads to good ductility, as observed in the present case. These results also point towards good strain-hardenability of the L1<sub>2</sub> phase which is presented in the next section.

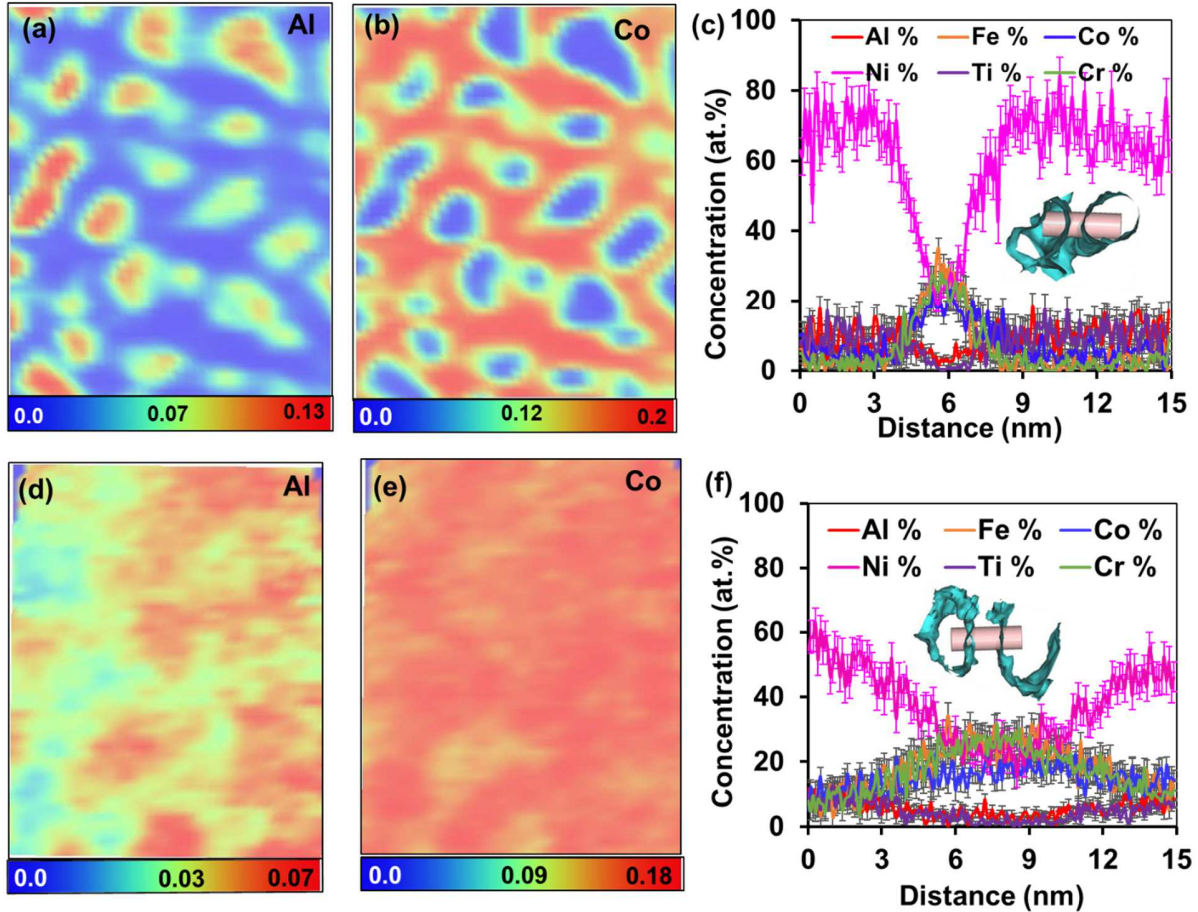


**Figure 10: APT results from the deformed CR-600 condition. A comparison of solute partitioning across the phase interface is done using a 2-D maps. (a-b) The 2-D compositional plots of Al and Co and (c) the 1-D compositional profile across the interface given in the inset. (d-e) The 2-D compositional plots of Al and Co and (f) the 1-D compositional profile across the interface given in the inset. Note the change from a sharp and stronger partitioning before deformation to a shallower and milder partitioning after deformation.**

#### Strain-hardenable multicomponent single L1<sub>2</sub> phase

The observed easy shearing of the  $\gamma'$  phase, following plastic deformation, indicates inherently good plasticity of the L1<sub>2</sub> phase. This is contrary to the conventional wisdom where ordered intermetallic compounds typically have impressive high temperature yield strengths but inherently low ductility and an overwhelming tendency of brittle failure. This has generally limited their usage as structural materials. Ductilizing these ordered intermetallic compounds to improve their tensile ductility involve myriad strategies such as engineering the grain-boundary

structure and chemistry, eliminating environmental embrittlement, promoting transformation-twinning-induced plasticity and so on [63–66].

We prepared a multicomponent intermetallic L<sub>1</sub><sub>2</sub> alloy with the nominal composition of the above-mentioned L<sub>1</sub><sub>2</sub> phase from the CR-600 condition (64Ni-6Co-2.5Fe-12Al-12Ti-3.5Cr at. %). Fig. 11 (a) is a diffraction pattern taken from this sample, along the [101] zone axis showing the superlattice spots corresponding to L<sub>1</sub><sub>2</sub> ordering. A DF TEM acquired from (10<sup>-</sup>1) superlattice reflection in Fig. 11 (b), convincingly shows single phase L<sub>1</sub><sub>2</sub> microstructure. Presence of isolated segments of growth dislocations is also evident. Fig. 11 (c) is a high-resolution image (HR-TEM image) with conclusively showing the ordered L<sub>1</sub><sub>2</sub> lattice. This single-phase multi-component intermetallic L<sub>1</sub><sub>2</sub> alloy was deformed under compressive loading (Fig. 11 (e)). The compressive stress-strain curve shows two extreme results out of five tested specimens. The yield-strength of the intermetallic alloy is 482+/-24 MPa while the plastic strain to failure varies from 25 % to 33 %. Most interestingly, the single-phase intermetallic alloy strain hardens from 486 MPa to 2130 MPa over a plastic strain of 25 % (From 480 MPa to 2450 over a plastic strain of 33 % in the second specimen). Such high strain hardenability in a single-phase intermetallic alloy is truly remarkable. To understand the deformation mechanism of this alloy, a TEM foil was prepared from the sample which was deformed to fracture. Fig. 11 (d) is a BF-TEM micrograph from this sample showing uniform and homogeneous dislocation activity within the bulk of the sample which correlates well with macroscopically observed good strain hardening in the alloy. The high strain hardenability of this L<sub>1</sub><sub>2</sub> ordered phase is also responsible for the good ductility in the CR-600 condition of the HEA being investigated in the present study. Very recently, Yang et al [37] reported a similar result of a ductile intermetallic compound with a complex multicomponent composition.

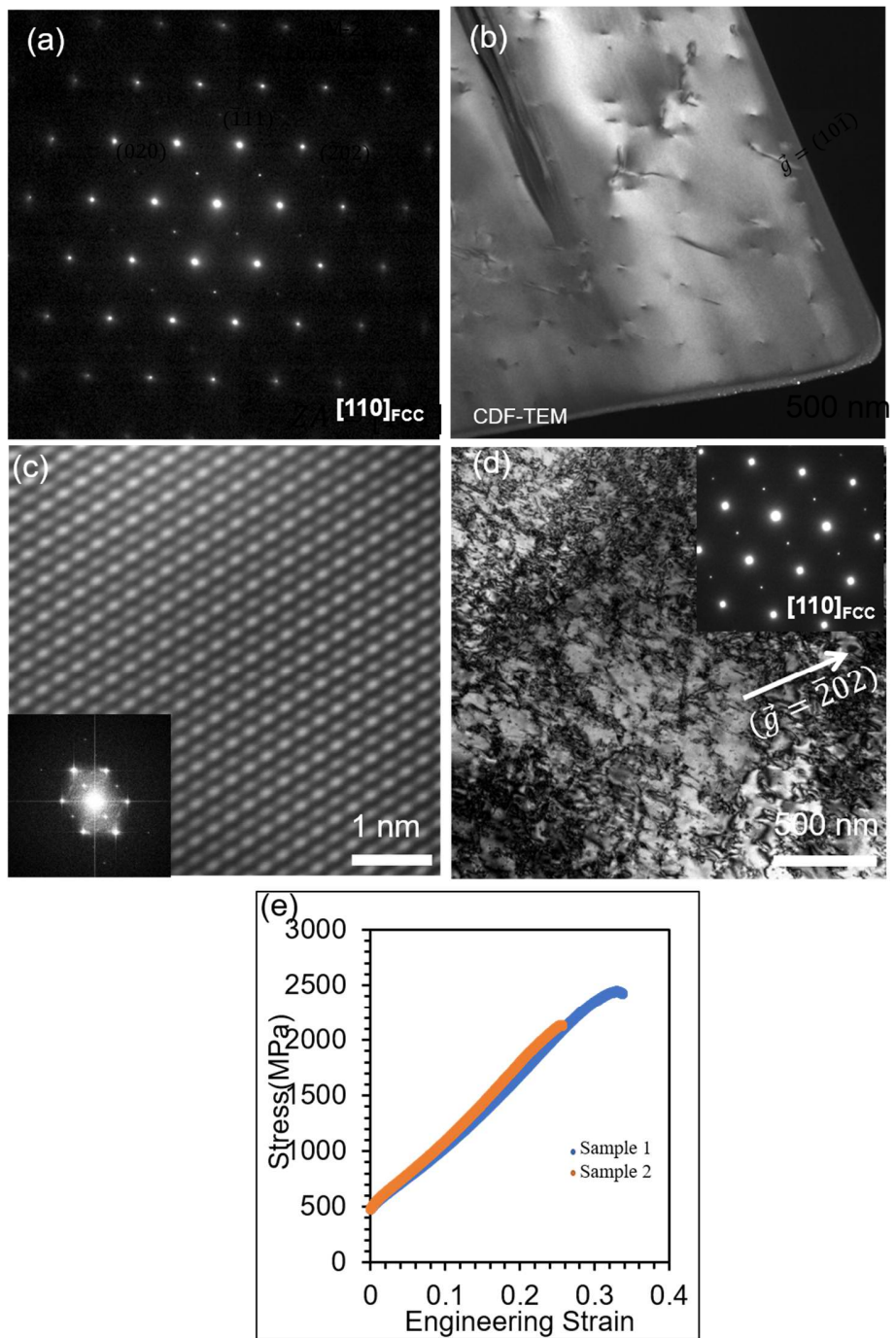


**Figure 11: Multicomponent intermetallic alloy:** A new alloy was prepared using the multicomponent composition from our high strength HEA. (a-d) TEM results conclusively show the single phase L1<sub>2</sub> crystal structure of the alloy. (a) SADP pattern with the strong superlattice spot at 011 and 001 positions. (b) CDF-TEM image showing single phase structure (c) HRTEM showing the atomic column image and (d) dislocation structure in the L1<sub>2</sub> phase. (e) Engineering stress-strain curves from 2 representative samples.

### Synergistic increase of strength while retaining ductility:

There are two major microstructural differences in the CR-600 and CR-800 alloy conditions:

- a) CR-600 has higher phase fraction of L<sub>1</sub><sub>2</sub> precipitates (~45 %) compared to CR-800 (~35 %). The size scale of the precipitates is also much finer in CR-600 compared to CR-800. Note, the average grain size distributions ( $1.0 \pm 0.2 \mu\text{m}$ ) in the two conditions are similar.
- b) The morphology of the L<sub>1</sub><sub>2</sub> precipitates changes from spherical in CR-800 to nano-rod like in CR-600.

These differences are reflected in the tensile deformation of the CR-600 and CR-800 conditions which are observed as an increase in the strength (from 1370 MPa in CR-800 to 1630 MPa in CR-600) while retaining a nominally similar ductility (12 % in CR-800 and 15% in CR-600) in the alloy. The increase in the strength of the alloy can be explained based on the higher precipitate density in CR-600 compared to the CR-800. Additionally, based on the work by Kelly et al [50], strengthenability from rod-like precipitates is 1.75 times higher compared to spherical precipitates. The mechanism for good ductility is the matrix-intermetallic deformability. We observed dislocation-mediated plasticity eventually leading to dislocation-dislocation interactions along with extensive shearing of precipitates. In addition, deformation twinning is observed traversing across matrix and precipitate thus accommodating strain without stress localization (Fig. 9 (f)). APT investigations revealed that tensile deformation of the discontinuous FCC + L<sub>1</sub><sub>2</sub> product leads to substantial shearing and intermixing across the FCC/L<sub>1</sub><sub>2</sub> nanorod interfaces. While the underlying rationale for such intermixing at room temperature requires further detailed investigation, this phenomenon appears to obviate any strong strain localization between the ordered L<sub>1</sub><sub>2</sub> phase and the disordered solid solution FCC phase. Consequently, the overall uniform tensile ductility of the HEA is preserved.

### **Summary and Conclusion**

Coupling compositional optimization guided by solution thermodynamics, together with thermo-mechanical processing, a new HEA has been designed which incorporates strong yet deformable ordered intermetallic (L<sub>1</sub><sub>2</sub>) nanorods within a complex concentrated *fcc* solid solution matrix. This HEA is a relatively low-cost alloy with an extremely high specific strength of 218 MPa/g/cc, as compared to specific strengths of Ni-based alloys (< 150 MPa/g/cm<sup>3</sup>) and most steels (< 200 MPa/g/ cm<sup>3</sup>) [57,67]. The present study results in the following summary points:

1. Typically, in traditional precipitation strengthened alloys, the strong intermetallic regions are discrete spherical/ellipsoidal/cuboidal shaped particles/precipitates uniformly distributed within the metallic solid solution matrix. Employing a unique thermo-mechanical processing route consisting of cold rolling and thermal annealing at the precipitation temperature, we have designed a novel microstructure consisting of intermetallic nanorods uniformly distributed within ultrafine scale (sub-micron) grains of a metallic solid solution.

2. This processing route also results in a substantially large fraction (~26.5%) of twin-related micron-sized grains, aiding in the subsequent room temperature plastic deformation of this HEA.
3. These intermetallic nanorods, dispersed within micron-sized grains of the metallic solid solution matrix, lead to the exceptionally high strength (~1.6 GPa) while retaining substantial deformability, leading to a tensile ductility of 15% strain to failure at room temperature.
4. The plastic deformation of this ultrahigh strength HEA is dominated by dislocation-mediated mechanisms coupled with limited deformation twinning. The high dislocation activity within the micron-sized grains, coupled with repeated shearing of the deformable intermetallic nanorods, results in good room temperature ductility.
5. Intermetallic compounds are typically very strong but are not deformable at room temperatures. However, the intermetallic compounds found in these HEAs can have complex compositions and substantial room temperature deformability or plasticity. This has been conclusively established via mechanical testing of the specific intermetallic compound forming in the HEA developed in the present study.

Furthermore, from a cost perspective, the high Fe concentration in the alloy reduces the raw material cost compared to conventional Ni-base super alloys. Based on current raw material costs, our alloy is estimated to cost ~\$5.5/lb as compared to the most commercial Ni-base super alloys whose costs lies in the range of \$7-12\$/lb [68].

Our strategy of developing precipitation strengthened alloy with unconventional rod-shaped multi-principal element based deformable intermetallic precipitates is a new design paradigm for alloys, and can be extended to many other alloy systems, such as steels, nickel or cobalt base superalloys, to achieve enhanced properties desired for many engineering applications. Using such design approaches, it is expected that a new generation of HEAs/CCAs will emerge with superior structural properties for advanced engineering systems, including automotive applications, high speed commuter transport, cryogenic devices, and aerospace systems.

### **Acknowledgements**

The work was supported by cooperative agreement between the US Army Research Laboratory and the University of North Texas [grant number W911NF-16-2-0189], and the US Air Force

Office of Scientific Research [grant number FA9550-17-1-0395]. BG would like to acknowledge the open call Laboratory Directed Research and Development programme at Pacific Northwest National Laboratory (PNNL). PNNL is operated for the U.S. DOE by Battelle Memorial Institute under Contract No. DE-AC05-76RLO1830. The authors acknowledge the Materials Research Facility (MRF) at the University of North Texas for use of microscopy facilities.

### Competing interests

We declare that none of the authors have competing financial or non-financial interests.

### Data availability

All relevant data supporting the key findings of this study are available within the article and its Supplementary Information files or from the corresponding author upon reasonable request.

### References

- [1] D.B. Miracle, O.N. Senkov, A critical review of high entropy alloys and related concepts, *Acta Mater.* 122 (2017) 448–511. <https://doi.org/10.1016/j.actamat.2016.08.081>.
- [2] E.P. George, D. Raabe, R.O. Ritchie, High-entropy alloys, *Nat. Rev. Mater.* 4 (2019) 515–534. <https://doi.org/10.1038/s41578-019-0121-4>.
- [3] Y. Shi, B. Yang, P.K. Liaw, Corrosion-resistant high-entropy alloys: A review, *Metals (Basel)*. 7 (2017). <https://doi.org/10.3390/met7020043>.
- [4] J. Li, Q. Zhang, R. Huang, X. Li, H. Gao, Towards understanding the structure–property relationships of heterogeneous-structured materials, *Scr. Mater.* 186 (2020) 304–311. <https://doi.org/10.1016/j.scriptamat.2020.05.013>.
- [5] X. Li, L. Lu, J. Li, X. Zhang, H. Gao, Mechanical properties and deformation mechanisms of gradient nanostructured metals and alloys, *Nat. Rev. Mater.* 5 (2020) 706–723. <https://doi.org/10.1038/s41578-020-0212-2>.
- [6] P. Shi, W. Ren, T. Zheng, Z. Ren, X. Hou, J. Peng, P. Hu, Y. Gao, Y. Zhong, P.K. Liaw, Enhanced strength–ductility synergy in ultrafine-grained eutectic high-entropy alloys by inheriting microstructural lamellae, *Nat. Commun.* 10 (2019) 1–8. <https://doi.org/10.1038/s41467-019-08460-2>.
- [7] J.Y. He, H. Wang, H.L. Huang, X.D. Xu, M.W. Chen, Y. Wu, X.J. Liu, T.G. Nieh, K. An, Z.P. Lu, A precipitation-hardened high-entropy alloy with outstanding tensile properties, *Acta Mater.* 102 (2016) 187–196. <https://doi.org/10.1016/j.actamat.2015.08.076>.
- [8] Y.J. Liang, L. Wang, Y. Wen, B. Cheng, Q. Wu, T. Cao, Q. Xiao, Y. Xue, G. Sha, Y. Wang, Y. Ren, X. Li, L. Wang, F. Wang, H. Cai, High-content ductile coherent nanoprecipitates achieve ultrastrong high-entropy alloys, *Nat. Commun.* 9 (2018) 1–8.

<https://doi.org/10.1038/s41467-018-06600-8>.

- [9] D.B. Williams, E.P. Butler, Grain boundary discontinuous precipitation reactions, *Int. Met. Rev.* (1981). <https://doi.org/10.1179/imtr.1981.26.1.153>.
- [10] I. Manna, S.K. Pabi, W. Gust, Discontinuous reactions in solids, *Int. Mater. Rev.* (2001). <https://doi.org/10.1179/095066001101528402>.
- [11] C.G. Ferguson, K.A. Christofidou, E.M. Hildyard, A.S. Wilson, N.G. Jones, H.J. Stone, On the continuous and discontinuous precipitation of the L1<sub>2</sub> phase in Cu-Ni-Al alloys, *Materialia*. 13 (2020). <https://doi.org/10.1016/j.mtla.2020.100855>.
- [12] Y. Liao, M. Xie, H. Chen, W. Xie, H. Wang, B. Yang, Thermodynamics and kinetics of discontinuous precipitation in Cu–9Ni–xSn alloy, *J. Alloys Compd.* 827 (2020). <https://doi.org/10.1016/j.jallcom.2020.154314>.
- [13] S.L. Chen, S. Daniel, F. Zhang, Y.A. Chang, X.Y. Yan, F.Y. Xie, R. Schmid-Fetzer, W.A. Oates, The PANDAT software package and its applications, *Calphad Comput. Coupling Phase Diagrams Thermochem.* 26 (2002) 175–188. [https://doi.org/10.1016/S0364-5916\(02\)00034-2](https://doi.org/10.1016/S0364-5916(02)00034-2).
- [14] J.O. Andersson, T. Helander, L. Höglund, P. Shi, B. Sundman, Thermo-Calc & DICTRA, computational tools for materials science, *Calphad Comput. Coupling Phase Diagrams Thermochem.* (2002). [https://doi.org/10.1016/S0364-5916\(02\)00037-8](https://doi.org/10.1016/S0364-5916(02)00037-8).
- [15] H.P. Chou, Y.S. Chang, S.K. Chen, J.W. Yeh, Microstructure, thermophysical and electrical properties in Al<sub>x</sub>CoCrFeNi ( $0 \leq x \leq 2$ ) high-entropy alloys, *Mater. Sci. Eng. B Solid-State Mater. Adv. Technol.* 163 (2009) 184–189. <https://doi.org/10.1016/j.mseb.2009.05.024>.
- [16] B. Gwalani, V. Soni, M. Lee, S.A. Mantri, Y. Ren, R. Banerjee, Optimizing the coupled effects of Hall-Petch and precipitation strengthening in a Al 0 . 3 CoCrFeNi high entropy alloy, *Mater. Des.* 121 (2017) 254–260. <https://doi.org/10.1016/j.matdes.2017.02.072>.
- [17] B. Gwalani, S. Gorsse, D. Choudhuri, M. Styles, Y. Zheng, R.S. Mishra, R. Banerjee, Modifying transformation pathways in high entropy alloys or complex concentrated alloys via thermo-mechanical processing, *Acta Mater.* 153 (2018) 169–185. <https://doi.org/10.1016/j.actamat.2018.05.009>.
- [18] D. Choudhuri, S. Shukla, B. Gwalani, R. Banerjee, R.S. Mishra, Deformation induced intermediate metastable lattice structures facilitate ordered B2 nucleation in a fcc-based high entropy alloy, *Mater. Res. Lett.* 7 (2019) 40–46. <https://doi.org/10.1080/21663831.2018.1553212>.
- [19] J. Sato, T. Omori, K. Oikawa, I. Ohnuma, R. Kainuma, K. Ishida, Cobalt-base high-temperature alloys, *Science* (80-. ). 312 (2006) 90–91. <https://doi.org/10.1126/science.1121738>.
- [20] A. Suzuki, H. Inui, T.M. Pollock, L1<sub>2</sub>-Strengthened Cobalt-Base Superalloys, *Annu. Rev. Mater. Res.* 45 (2015) 345–368. <https://doi.org/10.1146/annurev-matsci-070214-021043>.
- [21] T.M. Pollock, J. Dibbern, M. Tsunekane, J. Zhu, A. Suzuki, New Co-based  $\gamma$ - $\gamma'$  High-

temperature alloys, JOM. 62 (2010) 58–63. <https://doi.org/10.1007/s11837-010-0013-y>.

- [22] B. Gwalani, V. Soni, D. Choudhuri, M. Lee, J.Y. Hwang, S.J. Nam, H. Ryu, S.H. Hong, R. Banerjee, Stability of ordered L1<sub>2</sub> and B2 precipitates in face centered cubic based high entropy alloys - Al0.3CoFeCrNi and Al0.3CuFeCrNi<sub>2</sub>, Scr. Mater. 123 (2016) 130–134. <https://doi.org/10.1016/j.scriptamat.2016.06.019>.
- [23] A. Sharma, B. Gwalani, S. Dasari, D. Choudhuri, Y.J. Chang, S. Gorsse, A.C. Yeh, R. Banerjee, Insights into Defect-Mediated Nucleation of Equilibrium B2 Phase in Face-Centered Cubic High-Entropy Alloys, JOM. (2021). <https://doi.org/10.1007/s11837-021-04754-3>.
- [24] K. Kumar, A. Pooleery, K. Madhusoodanan, R.N. Singh, J.K. Chakravartty, B.K. Dutta, R.K. Sinha, Use of miniature tensile specimen for measurement of mechanical properties, in: Procedia Eng., 2014: pp. 899–909. <https://doi.org/10.1016/j.proeng.2014.11.112>.
- [25] K. Kumar, A. Pooleery, K. Madhusoodanan, R.N. Singh, A. Chatterjee, B.K. Dutta, R.K. Sinha, Optimisation of thickness of miniature tensile specimens for evaluation of mechanical properties, Mater. Sci. Eng. A. 675 (2016) 32–43. <https://doi.org/10.1016/j.msea.2016.08.032>.
- [26] A. Kolhatkar, V. Karthik, G.M.S.K. Chaitanya, A. Kumar, D. Ramchandran, Development and validation of a miniature tensile specimen for determination of mechanical properties, J. Test. Eval. 47 (2019). <https://doi.org/10.1520/JTE20180294>.
- [27] A.S. Argon, J. Im, Separation of second phase particles in spheroidized 1045 steel, Cu-0.6pct Cr alloy, and maraging steel in plastic straining, Metall. Trans. A. 6 (1975) 839–851. <https://doi.org/10.1007/BF02672307>.
- [28] U.K. Viswanathan, G.K. Dey, M.K. Asundi, Precipitation hardening in 350 grade maraging steel, Metall. Trans. A. 24 (1993) 2429–2442. <https://doi.org/10.1007/BF02646522>.
- [29] Z.B. Jiao, J.H. Luan, M.K. Miller, Y.W. Chung, C.T. Liu, Co-precipitation of nanoscale particles in steels with ultra-high strength for a new era, Mater. Today. 20 (2017) 142–154. <https://doi.org/10.1016/j.mattod.2016.07.002>.
- [30] S. Dasari, A. Sarkar, A. Sharma, B. Gwalani, D. Choudhuri, V. Soni, S. Manda, I. Samajdar, R. Banerjee, Recovery of cold-worked Al0.3CoCrFeNi complex concentrated alloy through twinning assisted B2 precipitation, Acta Mater. 202 (n.d.) 448–462.
- [31] D.P. Field, L.T. Bradford, M.M. Nowell, T.M. Lillo, The role of annealing twins during recrystallization of Cu, Acta Mater. 55 (2007) 4233–4241. <https://doi.org/10.1016/j.actamat.2007.03.021>.
- [32] P. Yu, R. Feng, J. Du, S. Shinzato, J.P. Chou, B. Chen, Y.C. Lo, P.K. Liaw, S. Ogata, A. Hu, Phase transformation assisted twinning in a face-centered-cubic FeCrNiCoAl0.36 high entropy alloy, Acta Mater. 181 (2019) 491–500. <https://doi.org/10.1016/j.actamat.2019.10.012>.
- [33] T.H. Lee, H.Y. Ha, J.H. Jang, J.Y. Kang, J. Moon, J.Y. Park, C.H. Lee, S.J. Park, Self-twinning in solid-state decomposition, Acta Mater. 123 (2017) 197–205.

<https://doi.org/10.1016/j.actamat.2016.10.039>.

- [34] A. Perovic, G.R. Purdy, Discontinuous precipitation in CuCo alloys, *Acta Metall.* (1981). [https://doi.org/10.1016/0001-6160\(81\)90086-9](https://doi.org/10.1016/0001-6160(81)90086-9).
- [35] O.C. Hellman, J.A. Vandenbroucke, J. Rüsing, D. Isheim, D.N. Seidman, Analysis of three-dimensional atom-probe data by the proximity histogram, *Microsc. Microanal.* 6 (2000) 437–444. <https://doi.org/10.1007/s100050010051>.
- [36] A.R.P. Singh, S. Nag, S. Chattopadhyay, Y. Ren, J. Tiley, G.B. Viswanathan, H.L. Fraser, R. Banerjee, Mechanisms related to different generations of  $\gamma'$  precipitation during continuous cooling of a nickel base superalloy, *Acta Mater.* 61 (2013) 280–293.
- [37] T. Yang, Y.L. Zhao, Y. Tong, Z.B. Jiao, J. Wei, J.X. Cai, X.D. Han, D. Chen, A. Hu, J.J. Kai, K. Lu, Y. Liu, C.T. Liu, Multicomponent intermetallic nanoparticles and superb mechanical behaviors of complex alloys, *Science* (80-. ). (2018). <https://doi.org/10.1126/science.aas8815>.
- [38] D.A. Porter, K.E. Easterling, M.Y. Sherif, *Phase transformations in metals and alloys*, third edition, 2009.
- [39] S. Asgari, E. El-Danaf, S.R. Kalidindi, R.D. Doherty, Strain hardening regimes and microstructural evolution during large strain compression of low stacking fault energy fee alloys that form deformation twins, *Metall. Mater. Trans. A Phys. Metall. Mater. Sci.* 28 (1997) 1781–1795. <https://doi.org/10.1007/s11661-997-0109-3>.
- [40] S. Gangireddy, B. Gwalani, K. Liu, R. Banerjee, R.S. Mishra, Microstructures with extraordinary dynamic work hardening and strain rate sensitivity in Al0.3CoCrFeNi high entropy alloy, *Mater. Sci. Eng. A*. 734 (2018) 42–50.
- [41] B. Gwalani, D. Choudhuri, V. Soni, Y. Ren, M. Styles, J.Y. Hwang, S.J. Nam, H. Ryu, S.H. Hong, R. Banerjee, Cu assisted stabilization and nucleation of L12 precipitates in Al0.3CuFeCrNi2 fcc-based high entropy alloy, *Acta Mater.* (2017). <https://doi.org/10.1016/j.actamat.2017.02.053>.
- [42] A. Jagetia, M. Nartu, S. Dasari, A. Sharma, B. Gwalani, R. Banerjee, Ordering-mediated local nano-clustering results in unusually large Hall-Petch strengthening coefficients in high entropy alloys, *Mater. Res. Lett.* (2021).
- [43] R.L. Fleischer, D. Peckner, The strengthening of metals, *J. Franklin Inst.* 277 (1964) 619. [https://doi.org/10.1016/0016-0032\(64\)90388-6](https://doi.org/10.1016/0016-0032(64)90388-6).
- [44] S. Yoshida, T. Ikeuchi, T. Bhattacharjee, Y. Bai, A. Shibata, N. Tsuji, Effect of elemental combination on friction stress and Hall-Petch relationship in face-centered cubic high / medium entropy alloys, *Acta Mater.* 171 (2019) 201–215. <https://doi.org/10.1016/j.actamat.2019.04.017>.
- [45] J.Y. He, H. Wang, H.L. Huang, X.D. Xu, M.W. Chen, Y. Wu, X.J. Liu, T.G. Nieh, K. An, Z.P. Lu, A precipitation-hardened high-entropy alloy with outstanding tensile properties, *Acta Mater.* 102 (2016) 187–196. <https://doi.org/10.1016/j.actamat.2015.08.076>.
- [46] Y. Tong, D. Chen, B. Han, J. Wang, R. Feng, T. Yang, C. Zhao, Y.L. Zhao, W. Guo, Y.

- Shimizu, C.T. Liu, P.K. Liaw, K. Inoue, Y. Nagai, A. Hu, J.J. Kai, Outstanding tensile properties of a precipitation-strengthened FeCoNiCrTi0.2 high-entropy alloy at room and cryogenic temperatures, *Acta Mater.* 165 (2019) 228–240.  
<https://doi.org/10.1016/j.actamat.2018.11.049>.
- [47] C.E. Slone, C.R. LaRosa, C.H. Zenk, E.P. George, M. Ghazisaeidi, M.J. Mills, Deactivating deformation twinning in medium-entropy CrCoNi with small additions of aluminum and titanium, *Scr. Mater.* (2020).  
<https://doi.org/10.1016/j.scriptamat.2019.11.053>.
- [48] K. Ma, H. Wen, T. Hu, T.D. Topping, D. Isheim, D.N. Seidman, E.J. Lavernia, J.M. Schoenung, Mechanical behavior and strengthening mechanisms in ultrafine grain precipitation-strengthened aluminum alloy, *Acta Mater.* 62 (2014) 141–155.  
<https://doi.org/10.1016/j.actamat.2013.09.042>.
- [49] M. Vittori, A. Mignone, On the antiphase boundary energy of Ni<sub>3</sub>(Al, Ti) particles, *Mater. Sci. Eng.* (1985). [https://doi.org/10.1016/0025-5416\(85\)90107-7](https://doi.org/10.1016/0025-5416(85)90107-7).
- [50] P.M. Kelly, The effect of particle shape on dispersion hardening, *Scr. Metall.* (1972).  
[https://doi.org/10.1016/0036-9748\(72\)90120-2](https://doi.org/10.1016/0036-9748(72)90120-2).
- [51] R.R. Huang, Q. Zhang, X. Zhang, J.G. Li, T.Q. Cao, J.H. Yao, Y.F. Xue, H.J. Gao, X.Y. Li, Dynamic recrystallization-induced temperature insensitivity of yield stress in single-crystal Al<sub>1.2</sub>CrFeCoNi micropillars, *Sci. China Technol. Sci.* 64 (2021) 11–22.  
<https://doi.org/10.1007/s11431-020-1660-8>.
- [52] B. Gwalani, S. Gangireddy, Y. Zheng, V. Soni, R.S. Mishra, R. Banerjee, Influence of ordered L<sub>1</sub> 2 precipitation on strain-rate dependent mechanical behavior in a eutectic high entropy alloy, *Sci. Rep.* 9 (2019) 1–13. <https://doi.org/10.1038/s41598-019-42870-y>.
- [53] D.M. Knowles, Q.Z. Chen, Superlattice stacking fault formation and twinning during creep in γ/γ' single crystal superalloy CMSX-4, *Mater. Sci. Eng. A.* 340 (2003) 88–102.  
[https://doi.org/10.1016/S0921-5093\(02\)00172-7](https://doi.org/10.1016/S0921-5093(02)00172-7).
- [54] R.R. Unocic, N. Zhou, L. Kovarik, C. Shen, Y. Wang, M.J. Mills, Dislocation decorrelation and relationship to deformation microtwins during creep of a γ' precipitate strengthened Ni-based superalloy, *Acta Mater.* 59 (2011) 7325–7339.  
<https://doi.org/10.1016/j.actamat.2011.07.069>.
- [55] G.B. Viswanathan, S. Karthikeyan, P.M. Sarosi, R.R. Unocic, M.J. Mills, Microtwinning during intermediate temperature creep of polycrystalline Ni-based superalloys: Mechanisms and modelling, *Philos. Mag.* 86 (2006) 4823–4840.  
<https://doi.org/10.1080/14786430600767750>.
- [56] S. Karthikeyan, R.R. Unocic, P.M. Sarosi, G.B. Viswanathan, D.D. Whitis, M.J. Mills, Modeling microtwinning during creep in Ni-based superalloys, *Scr. Mater.* 54 (2006) 1157–1162. <https://doi.org/10.1016/j.scriptamat.2005.11.049>.
- [57] M. Kolbe, The high temperature decrease of the critical resolved shear stress in nickel-base superalloys, *Mater. Sci. Eng. A.* 319–321 (2001) 383–387.  
[https://doi.org/10.1016/S0921-5093\(01\)00944-3](https://doi.org/10.1016/S0921-5093(01)00944-3).

- [58] Y.B. Xu, W.L. Zhong, Y.J. Chen, L.T. Shen, Q. Liu, Y.L. Bai, M.A. Meyers, Shear localization and recrystallization in dynamic deformation of 8090 Al-Li alloy, *Mater. Sci. Eng. A*. 299 (2001) 287–295. [https://doi.org/10.1016/S0921-5093\(00\)01412-X](https://doi.org/10.1016/S0921-5093(00)01412-X).
- [59] Y. Yang, Y. Chen, L. Jiang, M. Li, Q. Zhang, T. Tang, Study on the characteristics and thermal stability of nanostructures in adiabatic shear band of 2195 Al-Li alloy, *Appl. Phys. A Mater. Sci. Process.* 121 (2015) 1277–1284. <https://doi.org/10.1007/s00339-015-9506-4>.
- [60] Y. Yang, S. Luo, H. Hu, T. Tang, Q. Zhang, Diffusive transformation at high strain rate: On instantaneous dissolution of precipitates in aluminum alloy during adiabatic shear deformation, *J. Mater. Res.* 31 (2016) 1220–1228. <https://doi.org/10.1557/jmr.2016.151>.
- [61] M.H. Colliander, G. Sundell, M. Thuvander, Complete precipitate dissolution during adiabatic shear localisation in a Ni-based superalloy, *Philos. Mag. Lett.* 100 (2020) 561–570. <https://doi.org/10.1080/09500839.2020.1820595>.
- [62] H. He, X. Wu, C. Sun, L. Li, Grain structure and precipitate variations in 7003-T6 aluminum alloys associated with high strain rate deformation, *Mater. Sci. Eng. A*. 745 (2019) 429–439. <https://doi.org/10.1016/j.msea.2019.01.003>.
- [63] J.H. Westbrook, R.L. Fleischer, *Intermetallic Compounds, Principles and Practice*. Vol. 1 and 2, Wiley, John Sons Ltd, Baffins Lane, Chichester, Sussex PO 19 1 UD, UK, 1994. 1900. (1994).
- [64] HIGH-TEMPERATURE ORDERED INTERMETALLIC ALLOYS., *Mater. Res. Soc. Symp. Proc.* 39 (1985). <https://doi.org/10.1557/proc-81-3>.
- [65] K. Gschneidner, A. Russell, A. Pecharsky, J. Morris, Z. Zhang, T. Lograsso, D. Hsu, C.H.C. Lo, Y. Ye, A. Slager, D. Kesse, A family of ductile intermetallic compounds, *Nat. Mater.* 2 (2003) 587–590. <https://doi.org/10.1038/nmat958>.
- [66] Q. Li, S. Xue, J. Wang, S. Shao, A.H. Kwong, A. Giwa, Z. Fan, Y. Liu, Z. Qi, J. Ding, H. Wang, J.R. Greer, H. Wang, X. Zhang, High-Strength Nanotwinned Al Alloys with 9R Phase, *Adv. Mater.* 30 (2018). <https://doi.org/10.1002/adma.201704629>.
- [67] Y.J. Liang, L. Wang, Y. Wen, B. Cheng, Q. Wu, T. Cao, Q. Xiao, Y. Xue, G. Sha, Y. Wang, Y. Ren, X. Li, L. Wang, F. Wang, H. Cai, High-content ductile coherent nanoprecipitates achieve ultrastrong high-entropy alloys, *Nat. Commun.* 9 (2018). <https://doi.org/10.1038/s41467-018-06600-8>.
- [68] Metal and Alloy prices, 2020. <https://agmetalminer.com/metal-prices/>.

